

Tangent Space Approach for Thermal Tensor Network Simulations of the 2D Hubbard Model

Qiaoyi Li,^{1,2,3} Yuan Gao,^{1,2} Yuan-Yao He,^{4,5,3} Yang Qi,^{6,7,3,*} Bin-Bin Chen,^{8,†} and Wei Li^{2,3,9,10,‡}

¹*School of Physics, Beihang University, Beijing 100191, China*

²*CAS Key Laboratory of Theoretical Physics, Institute of Theoretical Physics, Chinese Academy of Sciences, Beijing 100190, China*

³*Hefei National Laboratory, University of Science and Technology of China, Hefei 230088, China*

⁴*Institute of Modern Physics, Northwest University, Xi'an 710127, China*

⁵*Shaanxi Key Laboratory for Theoretical Physics Frontiers, Xi'an 710127, China*

⁶*State Key Laboratory of Surface Physics and Department of Physics, Fudan University, Shanghai 200433, China*

⁷*Collaborative Innovation Center of Advanced Microstructures, Nanjing 210093, China*

⁸*Department of Physics and HKU-UCAS Joint Institute of Theoretical and Computational Physics, The University of Hong Kong, Pokfulam Road, Hong Kong, China*

⁹*Peng Huanwu Collaborative Center for Research and Education, Beihang University, Beijing 100191, China*

¹⁰*CAS Center for Excellence in Topological Quantum Computation, University of Chinese Academy of Sciences, Beijing 100190, China*

(Dated: June 7, 2023)

Accurate simulations of the two-dimensional (2D) Hubbard model constitute one of the most challenging problems in condensed matter and quantum physics. Here we develop a tangent space tensor renormalization group (tanTRG) approach for the calculations of the 2D Hubbard model at finite temperature. An optimal evolution of the density operator is achieved in tanTRG with a mild $O(D^3)$ complexity, where the bond dimension D controls the accuracy. With the tanTRG approach we boost the low-temperature calculations of large-scale 2D Hubbard systems on up to a width-8 cylinder and 10×10 square lattice. For the half-filled Hubbard model, the obtained results are in excellent agreement with those of determinant quantum Monte Carlo (DQMC). Moreover, tanTRG can be used to explore the low-temperature, finite-doping regime inaccessible for DQMC. The calculated charge compressibility and Matsubara Green's function are found to reflect the strange metal and pseudogap behaviors, respectively. The superconductive pairing susceptibility is computed down to a low temperature of approximately $1/24$ of the hopping energy, where we find d -wave pairing responses are most significant near the optimal doping. Equipped with the tangent-space technique, tanTRG constitutes a well-controlled, highly efficient and accurate tensor network method for strongly correlated 2D lattice models at finite temperature.

Introduction.— The paradigmatic Hubbard model [1, 2] is arguably the most intensively studied lattice model for strongly correlated electrons [3, 4]. It has been widely believed to capture the quintessence of high-temperature superconductivity [5–9], and recently also realized in optical lattice quantum simulations [10–15]. The intriguing interplay between the spin and charge degrees of freedom in the Hubbard model may give rise to abundant, even a plethora of electron orders in the finite-temperature phase diagram [16–21]. However, large-scale simulations of the 2D Hubbard model with a broad range of doping and down to low temperature yet constitute a widely open and truly challenging problem [4].

Tensor networks (TNs) and their renormalization group methods provide powerful approaches for quantum many-body problems [22–25]. In particular, thermal TNs [26–31] have been conceived and extensively used in the studies of low-dimensional quantum magnets [32–37] and recently also in correlated fermions at finite temperature [17, 38–42]. However, the accessible system size and lowest temperature that fermion thermal TN methods can handle are still rather limited. For a comparison, while the $T = 0$ density matrix renormalization group (DMRG) can deal with fermion cylinders of width $W = 6-8$ [43–46], finite-temperature calculations can currently reach a $W = 4$ Hubbard cylinder [17, 40]. For cracking electron secrets in the phase diagram of the 2D Hubbard model, like the strange metallicity [16], pseudogap [17], and d -wave superconductivity [46–50], further developments

in the algorithm are highly required.

In this work, we propose a tangent space tensor renormalization group (tanTRG) approach for highly controlled simulations both at half filling and finite doping. It has the following promising features: (i) A versatile 2D finite-temperature approach with efficient temperature grid design. Through a quasi-1D mapping, it systematically deals with the long-range interactions and evolves 2D systems based on the matrix product operator (MPO) representation of the Hamiltonian, making it advantageous over the Trotter-based approach [26, 27, 30, 51]. In tanTRG we integrate a flow equation and have a very high degree of flexibility in designing temperature grids. A remarkably larger imaginary-time step can be taken in tanTRG compared to Trotter-based approaches. (ii) Moderate computational complexity. Compared to the exponential tensor renormalization group (XTRG) that can simulate a 2D system down to low temperatures with a relatively high cost of $O(D^4)$ [29, 39], tanTRG is with only $O(D^3)$ complexity that allows for a significantly larger bond dimension D in the calculations. These advantages therefore lead to (iii) unprecedented finite-temperature simulations of large-scale systems. As fermion symmetries can be conveniently implemented in tanTRG with the tensor library QSpace [52–54], it further reduces the computational costs and allows for up to $D^* = 4,096 \text{ SU}(2)_{\text{charge}} \times \text{SU}(2)_{\text{spin}}$ multiplets at half filling (i.e., approximately $D \approx 25,000$ equivalent $\text{U}(1)_{\text{charge}} \times \text{U}(1)_{\text{spin}}$ states). For doped cases, $\text{U}(1)_{\text{charge}} \times \text{SU}(2)_{\text{spin}}$ can also be im-

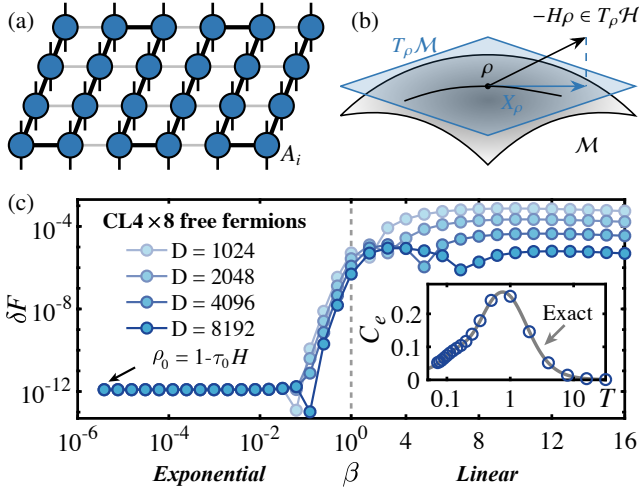


FIG. 1. (a) The MPO representation of thermal density operator ρ and corresponding quasi-1D mapping of the square lattice. The MPO consists of rank-4 tensors A_i with two geometric and two physical indices. (b) The MPO manifold \mathcal{M} and its tangent space $T_\rho \mathcal{M}$, where the black arrow denotes the tangent vector $-H\rho$ for imaginary-time evolution, and the blue one is its component within the tangent space $T_\rho \mathcal{M}$. The flow induced by the projected tangent vector field is indicated by the trajectory within the manifold \mathcal{M} . (c) The relative error $\delta F = |F - F_{\text{ex}}|/|F_{\text{ex}}|$ (with F_{ex} the exact solution) for half-filled free fermions on a 4×8 cylinder. A high accuracy is obtained by a hybrid cooling scheme with both exponential ($\beta \leq 1$) and linear ($\beta > 1$) temperature grids. There are two dips in δF that represent cancellation points between different types of errors (see analysis in SM [55]), and the inset shows the specific heat C_v in excellent agreement with the exact solution.

plemented. Note the spin and charge symmetries can be implemented in the MPO representation of the grand canonical ensemble (GCE) density operator. It helps further enhance the effective bond dimension D and renders excellent accuracy for large-scale Hubbard systems on up to a width-8 cylinder and 10×10 square lattice down to sufficiently low temperature.

Tangent space tensor renormalization group.— Finite-temperature properties are determined by the (unnormalized) density operator $\rho = e^{-\beta H}$ as illustrated in Fig. 1(a), with β the inverse temperature. The imaginary-time evolution equation reads $d\rho/d\beta = -H\rho$, with $-H\rho$ the tangent vector in $T_\rho \mathcal{H}$ (i.e., the tangent space of the full Hilbert space \mathcal{H}), which, in general, sticks out of the tangent space $T_\rho \mathcal{M}$ of the MPO manifold \mathcal{M} [see Fig. 1(b)], i.e., the MPO representation of ρ will increase its bond dimension D in the course of induced flow. In conventional thermal TN methods [26, 29–31, 51], the so-called truncation process is introduced to bring the evolved MPO back to manifold \mathcal{M} with a fixed D .

Alternatively, here we propose to optimize ρ within the MPO manifold \mathcal{M} using the technique of the time-dependent variational principle (TDVP) [56–60], which was originally conceived for real-time evolutions of pure quantum states. For a generalization to density operator ρ , we find the optimal tan-

gent vector X_ρ on the tangent space $T_\rho \mathcal{M}$, i.e.,

$$\frac{d\rho}{d\beta} = \arg \min_{X_\rho \in T_\rho \mathcal{M}} \|X_\rho + H\rho\|, \quad (1)$$

which defines a tangent vector field $\rho \mapsto X_\rho$ that induces the flow of $\rho(\beta)$ exactly on the manifold \mathcal{M} . With the MPO parameterization of ρ , the imaginary-time flow equation can be expressed with local tensors (c.f., Supplemental Material (SM) [55])

$$\frac{dA_i}{d\beta} = -H_i^{(1)} A_i + A_i^L H_i^{(0)} S_i, \quad (2)$$

where $H_i^{(1)}$ is the one-site effective Hamiltonian acting on the on-site tensor A_i , and $H_i^{(0)}$ is the bond effective Hamiltonian acting on the bond tensor S_i .

Following the splitting method [61], we separate Eq. (2) into two linear equations $dA_i/d\beta = -H_i^{(1)} A_i$ and $dS_i/d\beta = H_i^{(0)} S_i$ regarding the site and bond updates, respectively, and then integrate the equations sequentially in a sitewise sweep to conduct the time evolution. Taking a left-to-right sweep as an example, we first update the local tensor $A_i(\beta_0 + \tau) = e^{-\tau H_i^{(1)}} A_i(\beta_0)$ with the Lanczos-based exponential method, then left-canonicalize A_i via a QR decomposition $A_i = A_i^L S_i$. Subsequently, we conduct backward evolution of bond tensor $S_i(\beta_0 + \tau) = e^{\tau H_i^{(0)}} S_i(\beta_0)$, associate it to A_{i+1} , and then move on to the next site. Such a sweep process naturally maintains the canonical form of the MPO [55], and guarantees an optimal approximation within its manifold \mathcal{M} .

2D Hubbard model on the square lattice.— We consider the single-band Hubbard model on a square lattice, whose Hamiltonian reads

$$H = -t \sum_{\langle i,j \rangle, \sigma} (c_{i\sigma}^\dagger c_{j\sigma} + \text{H.c.}) + U \sum_i n_{i\uparrow} n_{i\downarrow} - \mu \sum_i n_i, \quad (3)$$

where $t = 1$ is chosen as the energy scale, and μ controls the fermion filling n (or hole doping $\delta = 1 - n$). The on-site repulsion is fixed as $U = 8$ if not otherwise mentioned. The calculations are performed on the cylinder lattice (CL) wrapped around the circumference direction (width W) while left open along the longitudinal direction (length L), and also open square (OS) lattice with full open boundaries.

Benchmarks on noninteracting fermions.— We start with benchmarks on free fermions with $U = 0$. The tanTRG calculations can be initialized from a high-temperature density operator $\rho_0 = 1 - \tau_0 H$ with very small $\tau_0 \sim 10^{-6}$, where a compact representation of ρ_0 can be conveniently constructed from the MPO representation of the Hamiltonian [62–66]. After that, we cool down the system by integrating the flow equation, Eq. (2), following flexible temperature grids, and compute the finite-temperature properties from $\rho(\beta)$.

In practice, we always start with exponential grids and exploit the two-site update allowing the MPO bond dimension D to increase adaptively. Successively, a pretty large and constant step length $4\tau = 1$ is adopted in the linear evolution

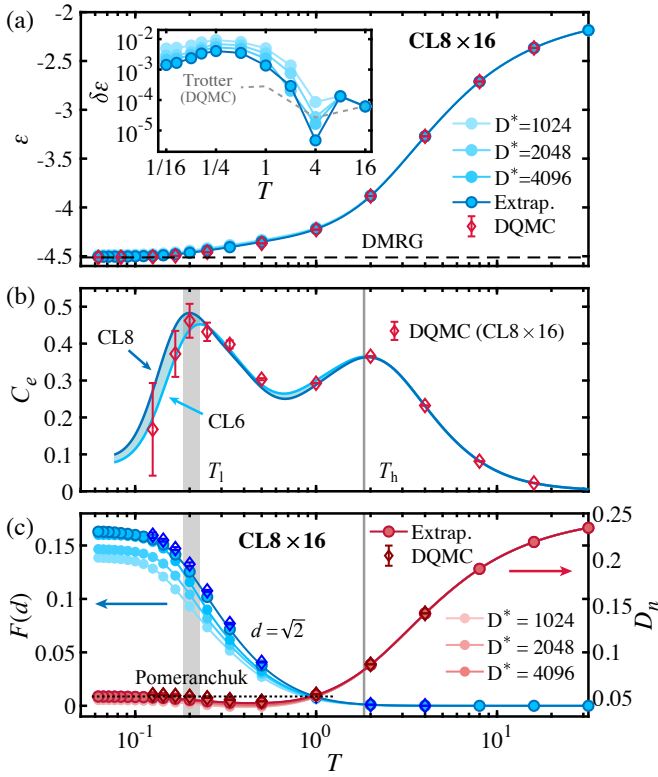


FIG. 2. (a) The results of the half-filled Hubbard model. The relative difference $\delta\varepsilon = \frac{|\varepsilon - \varepsilon_{\text{DQMC}}|}{|\varepsilon_{\text{DQMC}}|}$ of the tanTRG results (up to $D^* = 4096$ and extrapolated to infinite D) are plotted vs T in the inset, with the estimated Trotter errors of DQMC also indicated. The ground-state energy is obtained by standard two-site DMRG with $D^* = 8192$ (truncation error $\lesssim 10^{-5}$). (b) The electron specific heat C_e of CL6 \times 12 and CL8 \times 16, where the two C_e peaks indicate two temperature scales, namely, T_h and T_1 . (c) The double occupancy D_n and spin-spin correlations $F(d)$ with $d \equiv \sqrt{2}$, which change rapidly near T_h and T_1 , respectively. The anomalous decrease in D_n near T_1 as T rises reflects the Pomeranchuk effect in the Hubbard model.

stage. Very accurate results in free energy and specific heat are obtained in Fig. 1(c), as not only the projection but also Lie-Trotter errors are well controlled by bond dimension D [55]. Remember that the free fermion system, though being exactly soluble, poses challenges for TN methods due to the high entanglement associated with the Fermi surface (FS). Here the accurate results on free fermions show that tanTRG provides a powerful tool for tackling more realistic problems.

2D Hubbard model at half filling.— In Fig. 2, we present the tanTRG results on a width-8 cylinder CL8 \times 16, and leave the results on narrower cylinders ($W = 4, 6$) to the SM [55]. In practical calculations, we expand ρ_0 to higher orders [65] with a slightly larger $\tau_0 \sim 10^{-4}$, and a bilayer technique is used to compute thermodynamic quantities [67]. In Fig. 2(a) the results of the energy per site ε are found in excellent agreement with the determinant quantum Monte Carlo (DQMC) [68–71] data down to low temperature $T/t \approx 1/16$ [55].

With the extrapolated ε data, in Fig. 2(b) we show the computed specific heat $C_e = -\beta\partial\varepsilon/\partial\ln\beta$ again fully agrees with

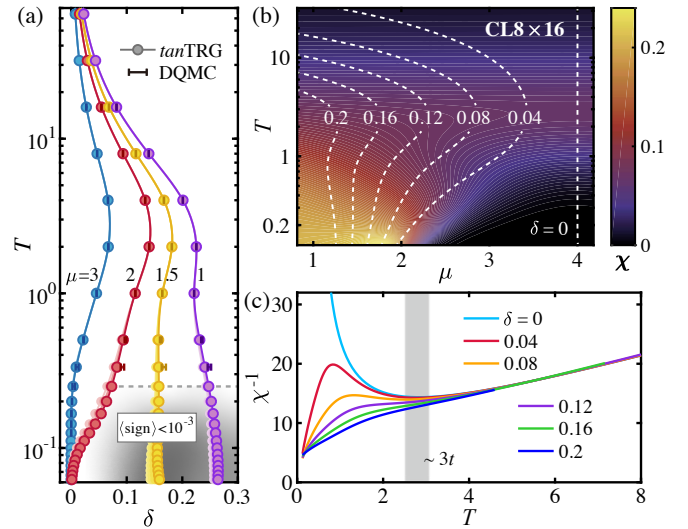


FIG. 3. (a) The doping δ for various T and μ . DQMC is accurate for the lightly doped case or at relatively higher temperature ($T/t > 0.3$) while it is hindered in the shaded regime with $\langle \text{sign} \rangle < 10^{-3}$. tanTRG offers accurate results even below $T/t \approx 0.06$, under a wide range of dopings. The extrapolation is based on the $D^* = 1024, 2048$ and 2896 data (and up to $D^* = 4096$ for $\mu = 1.5$ case), shown as translucent symbols. (b) The contour plot of compressibility χ , with the equal- δ (dashed) lines also indicated, and (c) plots the inverse compressibility χ^{-1} for various (interpolated) dopings δ .

the DQMC results. In particular, the two peaks in C_e , i.e., T_h and T_1 , respectively, for charge and spin peaks [72–74], constitute two-temperature scales. From the comparisons of CL6 and CL8 data, we find the higher charge peak $T_h/t \sim 2$ has fully converged to the thermodynamic limit and the lower spin peak $T_1/t \sim 0.2$ still changes slightly vs system widths.

As shown in Fig. 2(c), the double occupancy $D_n = \frac{1}{N} \sum_i \langle n_{i\uparrow} n_{i\downarrow} \rangle$ (with $N = L \times W$ the total site number) undergoes a rapid decrease at around T_h , indicating the onset of Mott physics. Upon further cooling, the spin-spin correlation $F(d) = \frac{1}{N_d} \sum_{\langle i,j \rangle_d} \langle S_i \cdot S_j \rangle$ (i.e., averaged over N_d pairs of sites separated by distance $|i - j| \equiv d$) rises up and becomes prominent below T_1 . Meanwhile, the double occupancy is found to exhibit a minimum at intermediate temperature $T_1 \lesssim T \lesssim T_h$ [74, 75]. This can be understood via the Maxwell’s relation $(\partial D_n / \partial T)_U = -(\partial S / \partial U)_T$, which associates the anomalous decrease in double occupancy as raising T with the increase of magnetic entropy upon localization by enhancing U . This constitutes an intriguing quantum phenomenon in the Mott phase of Hubbard model [76, 77] that resembles the renowned Pomeranchuk effect in ^3He .

Charge compressibility at finite doping.— Now we move on to the cases with finite doping. As GCE is adopted in tanTRG simulations, the hole doping δ varies with T and μ (for $\mu \neq U/2$) are shown in Fig. 3(a), again benchmarked with DQMC. For μ slightly lower than $U/2$, e.g., $\mu = 3$, δ approaches zero in the low temperature limit and the sign problem is not very critical for DQMC. In contrast, when μ further

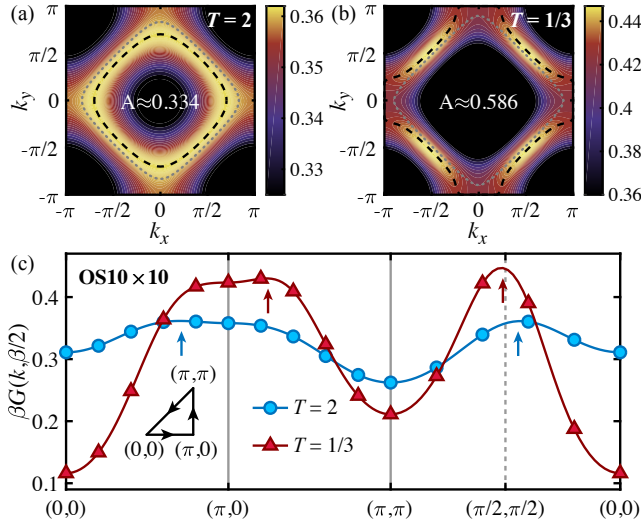


FIG. 4. Topography analysis of $\beta G(k, \beta/2)$ on OS 10×10 lattice with $\mu = 2$ for (a) $T = 2$ (with $\delta \simeq 0.14$) and (b) $T = 1/3$ ($\delta \simeq 0.064$), where the high-quality data are obtained with $D^* = 4096$. The dashed lines connect the maximum of $\beta G(k, \beta/2)$ and indicate the FS, whose enclosed area is denoted as A [with area of the first Brillouin zone (BZ) as unit 1]. The dotted line represents the FS in the noninteracting limit and with the same doping. (c) The triangular path in the BZ: At $T = 2$ the two maxima are located in the interval $[(0,0), (\pi,0)]$ and $[(\pi/2, \pi/2), (0,0)]$, indicating an electronlike FS; while for $T = 1/3$, the two maxima move respectively to the interval $[(\pi,0), (\pi, \pi)]$ and $[(\pi, \pi), (\pi/2, \pi/2)]$ for a holelike FS.

deviates $U/2$ and the doping level increases, the DQMC sign problem becomes severe (i.e., $\langle \text{sign} \rangle < 10^{-3}$, c.f., Supplemental Material Fig. S12 [55]).

As shown in Fig. 3(a), tanTRG produces accordant data in the regime where DQMC works well, and can “penetrate” into the shaded low- T regime inaccessible for DQMC. From Fig. 3(a) we note the electron density is most strongly fluctuating near $\delta \sim 0.1-0.2$, as evidenced by the large compressibility $\chi = (\partial n / \partial \mu)_T$ appearing at intermediate doping and low T in Figs. 3(b,c). We plot the inverse compressibility χ^{-1} in Fig. 3(c) for various dopings, where the χ^{-1} results exhibit universal linear- T behaviors for $T/t \gtrsim 3$ with little doping dependence. Considering that the compressibility χ has an intimate relation to dc resistivity via the Nernst-Einstein relation, the universal behaviors of χ^{-1} account for the linearity of resistivity in the high-temperature ($T/t \gtrsim 3$) regime. Below $T/t \sim 3$, distinct χ^{-1} behaviors of the Mott insulator and bad metals can be clearly observed. In particular, χ^{-1} is found to converge to a nonzero constant for $T/t \sim 0.1$, which is argued to be related to the second, doping-dependent linear- T regime of resistivity controlled instead by the diffusivity [16].

Matsubara Green’s function and Fermi surface topology.— Below the crossover temperature scale $T/t \sim 3$, the inverse compressibility χ^{-1} exhibits a maximum in Figs. 3(b,c) for the slightly doped case, e.g., $\delta = 0.04, 0.08$, which suggests a dramatic change in the FS upon cooling. For this we compute the single-particle Matsubara Green’s function $G(k, \beta/2) =$

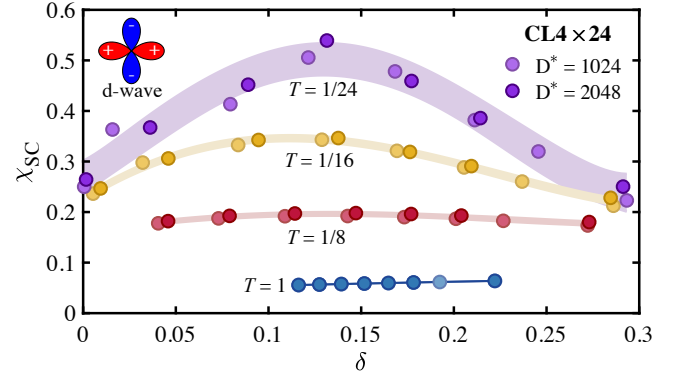


FIG. 5. Pairing susceptibility of the $CL4 \times 24$ Hubbard model with various dopings and temperatures. A pairing field $h_p = 0.01$ is adopted in the calculations, with non-Abelian $Z_{2, \text{charge}} \times SU(2)_{\text{spin}}$ symmetry implemented. The computed χ_{SC} vs δ fall into the background stripes estimated from the polynomial fittings, whose widths represent the $(\pm\sigma)$ confidence intervals.

$\sum_{\sigma} \langle e^{\beta H/2} c_{k\sigma}^{\dagger} e^{-\beta H/2} c_{k\sigma} \rangle_{\beta}$ with $c_{k\sigma} = \frac{1}{\sqrt{N}} \sum_r e^{-ikr} c_{r\sigma}$ [78] that reflects the spectral weight near the FS through $\beta G(k, \beta/2) \sim A(k, \omega = 0)$ at low temperature [79, 80]. In Fig. 4, we show the results of $\beta G(k, \beta/2)$ in a slightly doped case, and find quite peculiar temperature evolution of the FS. Despite some blurring due to thermal fluctuations, an electronlike FS with enclosed area $A < 1/2$ can be observed. As the temperature ramps down, an “interacting Lifshitz transition” [18, 81, 82] occurs. A holelike FS with enclosed area $A > 1/2$ appears in Fig. 4(b), with the boundary “pushed” outwards with respect to the free-fermion FS. The unexpected holelike FS seems to violate the Luttinger theorem and echoes the conclusion in Refs. [19, 20, 83, 84] — the FS topology change can be associated with the opening of a pseudogap. Moreover, we find the signature of the pseudogap gets clearer when the system size increases, and it becomes very prominent when a next nearest hopping t' is introduced [55].

d-wave pairing response.— Next we compute the superconductive pairing responses by applying a pairing field $-h_p \Delta_{\text{tot}} \equiv -h_p \sum_{\langle i,j \rangle} s_{ij} (\Delta_{ij} + \Delta_{ij}^{\dagger})/2$, where $\Delta_{ij} = (c_{i\downarrow} c_{j\uparrow} - c_{i\uparrow} c_{j\downarrow})/\sqrt{2}$, and $s_{ij} = 1(-1)$ for horizontal(vertical) bonds (c.f., inset in Fig. 5). The results of pairing susceptibility $\chi_{\text{SC}} = \frac{1}{N_p h_p} \langle \Delta_{\text{tot}} \rangle_T$ (with N_p the bond number) are shown in Fig. 5. At relatively high temperature, e.g., $T/t = 1$ and $1/8$, χ_{SC} values are small and insensitive to dopings. However, as the temperature further decreases to $T/t \lesssim 1/16$, χ_{SC} displays a domelike shape with prominent responses near optimal doping $\delta_x \approx 1/8$. Moreover, the induced superconductive order parameter $\frac{1}{N_p} \langle \Delta_{\text{tot}} \rangle_T$ is found to vanish as $h_p \rightarrow 0$, even for the lowest accessed temperature. Instead, charge stripes and spin correlation modulations appear for $T \lesssim 1/32$ [55]. These results, in full agreement with previous studies [21, 45, 85, 86], show that the ground-state features can be well captured by tanTRG calculations down to sufficiently low temperature.

Summary and outlook.— With tangent-space techniques,

we evolve the density operator ρ optimally on the MPO manifold and propose a powerful approach for exploring 2D many-electron problems. We study the intriguing behaviors of charge compressibility that reflect strange metallicity, and unveil a holelike FS in the pseudogap regime. The d -wave pairing responses are computed down to $T/t = 1/24$, which are otherwise rather challenging to obtain for the 2D Hubbard model.

This approach has a wide variety of features. It can reach a low-temperature doped regime that is inaccessible for DQMC, and the $O(D^3)$ complexity, together with the implementation of non-Abelian symmetries, enables tanTRG to deal with wide $W = 8$ cylinders at finite temperature. This is clearly beyond the current limit of $W = 4$ [17, 40], where tanTRG obtains results in agreement with minimally entangled typical thermal states (METTS)[17, 27, 28] (see comparisons in SM [55]). Overall, our results close the gap between thermal TN and ground-state DMRG calculations in terms of system size. As the cylinder width $W > 4$ is important for observing 2D correlation physics [45–50, 87], we believe tanTRG will play an active role in exploring the intriguing temperature-doping phase diagrams, and help establish solid connections between theories of high- T_c superconductivity with fundamental models of correlated electrons.

Acknowledgments.— The authors are indebted to Dai-Wei Qu, Shou-Shu Gong, Lei Wang, Wei Wu, Zi Yang Meng, and Tao Shi for helpful discussions. This work was supported by the National Natural Science Foundation of China (Grants No. 12222412, 11974036, 11834014, 12047503, 12204377 and 12174068), CAS Project for Young Scientists in Basic Research (Grant No. YSBR-057), and the Innovation Program for Quantum Science and Technology (under Grant No. 2021ZD0301900). We thank HPC at ITP-CAS and HPC2021 at the University of Hong Kong for the technical support and generous allocation of CPU time.

* qiyang@fudan.edu.cn

† bchenhku@hku.hk

‡ w.li@itp.ac.cn

- [1] J. Hubbard, Electron correlations in narrow energy bands, *Proc. R. Soc. A* **276**, 238 (1963).
- [2] M. C. Gutzwiller, Effect of Correlation on the Ferromagnetism of Transition Metals, *Phys. Rev. Lett.* **10**, 159 (1963).
- [3] D. P. Arovas, E. Berg, S. A. Kivelson, and S. Raghu, The Hubbard model, *Annu. Rev. Condens. Matter Phys.* **13**, 239 (2022).
- [4] M. Qin, T. Schäfer, S. Andergassen, P. Corboz, and E. Gull, The Hubbard model: A computational perspective, *Annu. Rev. Condens. Matter Phys.* **13**, 275 (2022).
- [5] J. G. Bednorz and K. A. Müller, Possible high T_c superconductivity in the Ba-La-Cu-O system, *Z. Phys. B* **64**, 189 (1986).
- [6] C. C. Tsuei and J. R. Kirtley, Pairing symmetry in cuprate superconductors, *Rev. Mod. Phys.* **72**, 969 (2000).
- [7] P. A. Lee, N. Nagaosa, and X.-G. Wen, Doping a Mott insulator: Physics of high-temperature superconductivity, *Rev. Mod. Phys.* **78**, 17 (2006).
- [8] B. Keimer, S. A. Kivelson, M. R. Norman, S. Uchida, and J. Zaanen, From quantum matter to high-temperature superconductivity in copper oxides, *Nature* **518**, 179 (2015).
- [9] C. Proust and L. Taillefer, The remarkable underlying ground states of cuprate superconductors, *Annu. Rev. Condens. Matter Phys.* **10**, 409 (2019).
- [10] M. F. Parsons, A. Mazurenko, C. S. Chiu, G. Ji, D. Greif, and M. Greiner, Site-resolved measurement of the spin-correlation function in the Fermi-Hubbard model, *Science* **353**, 1253 (2016).
- [11] D. Greif, M. F. Parsons, A. Mazurenko, C. S. Chiu, S. Blatt, F. Huber, G. Ji, and M. Greiner, Site-resolved imaging of a fermionic Mott insulator, *Science* **351**, 953 (2016).
- [12] L. W. Cheuk, M. A. Nichols, K. R. Lawrence, M. Okan, H. Zhang, E. Khatami, N. Trivedi, T. Paiva, M. Rigol, and M. W. Zwierlein, Observation of spatial charge and spin correlations in the 2D Fermi-Hubbard model, *Science* **353**, 1260 (2016).
- [13] A. Mazurenko, C. S. Chiu, G. Ji, M. F. Parsons, M. Kanász-Nagy, R. Schmidt, F. Grusdt, E. Demler, D. Greif, and M. Greiner, A cold-atom Fermi-Hubbard antiferromagnet, *Nature* **545**, 462 (2017).
- [14] J. Koepsell, D. Bourgund, P. Sompet, S. Hirthe, A. Bohrdt, Y. Wang, F. Grusdt, E. Demler, G. Salomon, C. Gross, and I. Bloch, Microscopic evolution of doped Mott insulators from polaronic metal to Fermi liquid, *Science* **374**, 82 (2021).
- [15] P. Sompet, S. Hirthe, D. Bourgund, T. Chalopin, J. Bibo, J. Koepsell, P. Bojović, R. Verresen, F. Pollmann, G. Salomon, C. Gross, T. A. Hilker, and I. Bloch, Realizing the symmetry-protected Haldane phase in Fermi-Hubbard ladders, *Nature* **606**, 484 (2022).
- [16] E. W. Huang, R. Sheppard, B. Moritz, and T. P. Devereaux, Strange metallicity in the doped Hubbard model, *Science* **366**, 987 (2019).
- [17] A. Wietek, Y.-Y. He, S. R. White, A. Georges, and E. M. Stoudenmire, Stripes, Antiferromagnetism, and the Pseudogap in the Doped Hubbard Model at Finite Temperature, *Phys. Rev. X* **11**, 031007 (2021).
- [18] A. N. Rubtsov, M. I. Katsnelson, A. I. Lichtenstein, and A. Georges, Dual fermion approach to the two-dimensional Hubbard model: Antiferromagnetic fluctuations and Fermi arcs, *Phys. Rev. B* **79**, 045133 (2009).
- [19] W. Wu, M. S. Scheurer, S. Chatterjee, S. Sachdev, A. Georges, and M. Ferrero, Pseudogap and Fermi-Surface Topology in the Two-Dimensional Hubbard Model, *Phys. Rev. X* **8**, 021048 (2018).
- [20] M. S. Scheurer, S. Chatterjee, W. Wu, M. Ferrero, A. Georges, and S. Sachdev, Topological order in the pseudogap metal, *Proc. Natl. Acad. Sci. U.S.A.* **115**, E3665 (2018).
- [21] B. Xiao, Y.-Y. He, A. Georges, and S. Zhang, Temperature Dependence of Spin and Charge Orders in the Doped Two-Dimensional Hubbard Model, *Phys. Rev. X* **13**, 011007 (2023).
- [22] S. R. White, Density Matrix Formulation for Quantum Renormalization Groups, *Phys. Rev. Lett.* **69**, 2863 (1992).
- [23] F. Verstraete, J. J. García-Ripoll, and J. I. Cirac, Matrix Product Density Operators: Simulation of Finite-Temperature and Dissipative Systems, *Phys. Rev. Lett.* **93**, 207204 (2004).
- [24] U. Schollwöck, The density-matrix renormalization group in the age of matrix product states, *Ann. Phys.* **326**, 96 (2011).
- [25] J. I. Cirac, D. Pérez-García, N. Schuch, and F. Verstraete, Matrix product states and projected entangled pair states: Concepts, symmetries, theorems, *Rev. Mod. Phys.* **93**, 045003 (2021).
- [26] A. E. Feiguin and S. R. White, Finite-temperature density ma-

- trix renormalization using an enlarged Hilbert space, *Phys. Rev. B* **72**, 220401(R) (2005).
- [27] S. R. White, Minimally Entangled Typical Quantum States at Finite Temperature, *Phys. Rev. Lett.* **102**, 190601 (2009).
- [28] E. M. Stoudenmire and S. R. White, Minimally entangled typical thermal state algorithms, *New Journal of Physics* **12**, 055026 (2010).
- [29] B.-B. Chen, L. Chen, Z. Chen, W. Li, and A. Weichselbaum, Exponential Thermal Tensor Network Approach for Quantum Lattice Models, *Phys. Rev. X* **8**, 031082 (2018).
- [30] W. Li, S.-J. Ran, S.-S. Gong, Y. Zhao, B. Xi, F. Ye, and G. Su, Linearized Tensor Renormalization Group Algorithm for the Calculation of Thermodynamic Properties of Quantum Lattice Models, *Phys. Rev. Lett.* **106**, 127202 (2011).
- [31] P. Czarnik, L. Cincio, and J. Dziarmaga, Projected entangled pair states at finite temperature: Imaginary time evolution with ancillas, *Phys. Rev. B* **86**, 245101 (2012).
- [32] T. Xiang, Thermodynamics of quantum Heisenberg spin chains, *Phys. Rev. B* **58**, 9142 (1998).
- [33] L. Chen, D.-W. Qu, H. Li, B.-B. Chen, S.-S. Gong, J. von Delft, A. Weichselbaum, and W. Li, Two-temperature scales in the triangular-lattice Heisenberg antiferromagnet, *Phys. Rev. B* **99**, 140404(R) (2019).
- [34] H. Li, Y. D. Liao, B.-B. Chen, X.-T. Zeng, X.-L. Sheng, Y. Qi, Z. Y. Meng, and W. Li, Kosterlitz-Thouless melting of magnetic order in the triangular quantum Ising material TmMgGaO₄, *Nat. Commun.* **11**, 1111 (2020).
- [35] H. Li, H.-K. Zhang, J. Wang, H.-Q. Wu, Y. Gao, D.-W. Qu, Z.-X. Liu, S.-S. Gong, and W. Li, Identification of magnetic interactions and high-field quantum spin liquid in α -RuCl₃, *Nat. Commun.* **12**, 4007 (2021).
- [36] S. Yu, Y. Gao, B.-B. Chen, and W. Li, Learning the Effective Spin Hamiltonian of a Quantum Magnet, *Chin. Phys. Lett.* **38**, 097502 (2021).
- [37] J. L. Jiménez, S. P. G. Crone, E. Fogh, M. E. Zayed, R. Lortz, E. Pomjakushina, K. Conder, A. M. Läuchli, L. Weber, S. Wessel, A. Honecker, B. Normand, C. Rüegg, P. Corboz, H. M. Rønnow, and F. Mila, A quantum magnetic analogue to the critical point of water, *Nature* **592**, 370 (2021).
- [38] P. Czarnik, M. M. Rams, and J. Dziarmaga, Variational tensor network renormalization in imaginary time: Benchmark results in the Hubbard model at finite temperature, *Phys. Rev. B* **94**, 235142 (2016).
- [39] B.-B. Chen, C. Chen, Z. Chen, J. Cui, Y. Zhai, A. Weichselbaum, J. von Delft, Z. Y. Meng, and W. Li, Quantum many-body simulations of the two-dimensional Fermi-Hubbard model in ultracold optical lattices, *Phys. Rev. B* **103**, L041107 (2021).
- [40] A. Wietek, R. Rossi, F. Šimkovic, M. Klett, P. Hansmann, M. Ferrero, E. M. Stoudenmire, T. Schäfer, and A. Georges, Mott Insulating States with Competing Orders in the Triangular Lattice Hubbard Model, *Phys. Rev. X* **11**, 041013 (2021).
- [41] X. Lin, B.-B. Chen, W. Li, Z. Y. Meng, and T. Shi, Exciton Proliferation and Fate of the Topological Mott Insulator in a Twisted Bilayer Graphene Lattice Model, *Phys. Rev. Lett.* **128**, 157201 (2022).
- [42] A. Sinha, M. M. Rams, P. Czarnik, and J. Dziarmaga, Finite-temperature tensor network study of the Hubbard model on an infinite square lattice, *Phys. Rev. B* **106**, 195105 (2022).
- [43] J. P. F. LeBlanc, A. E. Antipov, F. Becca, I. W. Bulik, G. K.-L. Chan, C.-M. Chung, Y. Deng, M. Ferrero, T. M. Henderson, C. A. Jiménez-Hoyos, E. Kozik, X.-W. Liu, A. J. Millis, N. V. Prokof'ev, M. Qin, G. E. Scuseria, H. Shi, B. V. Svistunov, L. F. Tocchio, I. S. Tupitsyn, S. R. White, S. Zhang, X. Zheng, Z. Zhu, and E. Gull (Simons Collaboration on the Many-Electron Problem), Solutions of the Two-Dimensional Hubbard Model: Benchmarks and Results from a Wide Range of Numerical Algorithms, *Phys. Rev. X* **5**, 041041 (2015).
- [44] B.-X. Zheng, C.-M. Chung, P. Corboz, G. Ehlers, M.-P. Qin, R. M. Noack, H. Shi, S. R. White, S. Zhang, and G. K.-L. Chan, Stripe order in the underdoped region of the two-dimensional Hubbard model, *Science* **358**, 1155 (2017).
- [45] M. Qin, C.-M. Chung, H. Shi, E. Vitali, C. Hubig, U. Schollwöck, S. R. White, and S. Zhang (Simons Collaboration on the Many-Electron Problem), Absence of Superconductivity in the Pure Two-Dimensional Hubbard Model, *Phys. Rev. X* **10**, 031016 (2020).
- [46] S. Jiang, D. J. Scalapino, and S. R. White, Ground-state phase diagram of the $t-t'-J$ model, *Proc. Natl. Acad. Sci. U.S.A.* **118**, e2109978118 (2021).
- [47] H. C. Jiang and T. P. Devereaux, Superconductivity in the doped Hubbard model and its interplay with next-nearest hopping t' , *Science* **365**, 1424 (2019).
- [48] Y.-F. Jiang, J. Zaanen, T. P. Devereaux, and H.-C. Jiang, Ground state phase diagram of the doped Hubbard model on the four-leg cylinder, *Phys. Rev. Res.* **2**, 033073 (2020).
- [49] H.-C. Jiang and S. A. Kivelson, High Temperature Superconductivity in a Lightly Doped Quantum Spin Liquid, *Phys. Rev. Lett.* **127**, 097002 (2021).
- [50] S. Gong, W. Zhu, and D. N. Sheng, Robust d -wave Superconductivity in the Square-Lattice $t-J$ Model, *Phys. Rev. Lett.* **127**, 097003 (2021).
- [51] M. Zwolak and G. Vidal, Mixed-State Dynamics in One-Dimensional Quantum Lattice Systems: A Time-Dependent Superoperator Renormalization Algorithm, *Phys. Rev. Lett.* **93**, 207205 (2004).
- [52] A. Weichselbaum, Non-abelian symmetries in tensor networks: A quantum symmetry space approach, *Ann. Phys.* **327**, 2972 (2012).
- [53] A. Weichselbaum, X-Symbols for non-Abelian symmetries in tensor networks, *Phys. Rev. Res.* **2**, 023385 (2020).
- [54] B. Bruognolo, J.-W. Li, J. von Delft, and A. Weichselbaum, A beginner's guide to non-abelian iPEPS for correlated fermions, *SciPost Phys. Lect. Notes*, 25 (2021).
- [55] Supplemental Material. Section I shows *tan*TRG results on width-4 and 6 cylinders, Matsubara Green's function, d -wave pairing responses, spin and charge correlations, and the numerical error analysis. Section II describes the MPO flow equation, Lanczos-based exponential method, and the Lie-Trotter splitting. Section III is devoted to details of the DQMC calculations. The Supplemental Material includes Refs. [88–91].
- [56] J. Haegeman, J. I. Cirac, T. J. Osborne, I. Pižorn, H. Verschelde, and F. Verstraete, Time-Dependent Variational Principle for Quantum Lattices, *Phys. Rev. Lett.* **107**, 070601 (2011).
- [57] J. Haegeman, M. Mariën, T. J. Osborne, and F. Verstraete, Geometry of matrix product states: Metric, parallel transport, and curvature, *J. Math. Phys.* **55**, 021902 (2014).
- [58] J. Haegeman, C. Lubich, I. Oseledets, B. Vandereycken, and F. Verstraete, Unifying time evolution and optimization with matrix product states, *Phys. Rev. B* **94**, 165116 (2016).
- [59] M. Yang and S. R. White, Time-dependent variational principle with ancillary Krylov subspace, *Phys. Rev. B* **102**, 094315 (2020).
- [60] L. Hackl, T. Guaita, T. Shi, J. Haegeman, E. Demler, and J. I. Cirac, Geometry of variational methods: Dynamics of closed quantum systems, *SciPost Phys.* **9**, 048 (2020).
- [61] E. Hairer, G. Wanner, and C. Lubich, *Geometric Numerical Integration*, 2nd ed. (Springer Berlin, Heidelberg, 2006).

- [62] F. Fröwis, V. Nebendahl, and W. Dür, Tensor operators: Constructions and applications for long-range interaction systems, *Phys. Rev. A* **81**, 062337 (2010).
- [63] B. Pirvu, V. Murg, J. I. Cirac, and V. F., Matrix product operator representations, *New J. Phys.* **12**, 025012 (2010).
- [64] C. Hubig, I. P. McCulloch, and U. Schollwöck, Generic construction of efficient matrix product operators, *Phys. Rev. B* **95**, 035129 (2017).
- [65] B.-B. Chen, Y.-J. Liu, Z. Chen, and W. Li, Series-expansion thermal tensor network approach for quantum lattice models, *Phys. Rev. B* **95**, 161104(R) (2017).
- [66] B.-B. Chen, L. Chen, Z. Chen, W. Li, and A. Weichselbaum, Exponential Thermal Tensor Network Approach for Quantum Lattice Models, *Phys. Rev. X* **8**, 031082 (2018).
- [67] Y.-L. Dong, L. Chen, Y.-J. Liu, and W. Li, Bilayer linearized tensor renormalization group approach for thermal tensor networks, *Phys. Rev. B* **95**, 144428 (2017).
- [68] R. Blankenbecler, D. J. Scalapino, and R. L. Sugar, Monte Carlo calculations of coupled boson-fermion systems. I, *Phys. Rev. D* **24**, 2278 (1981).
- [69] J. E. Hirsch, Discrete Hubbard-Stratonovich transformation for fermion lattice models, *Phys. Rev. B* **28**, 4059 (1983).
- [70] J. E. Hirsch, Two-dimensional Hubbard model: Numerical simulation study, *Phys. Rev. B* **31**, 4403 (1985).
- [71] F. Assaad and H. Evertz, World-Line and Determinantal Quantum Monte Carlo Methods for Spins, Phonons and Electrons, in *Computational Many-Particle Physics*, edited by H. Fehske, R. Schneider, and A. Weiße (Springer Berlin Heidelberg, Berlin, Heidelberg, 2008) pp. 277–356.
- [72] D. Duffy and A. Moreo, Specific heat of the two-dimensional Hubbard model, *Phys. Rev. B* **55**, 12918 (1997).
- [73] T. Paiva, R. T. Scalettar, C. Huscroft, and A. K. McMahan, Signatures of spin and charge energy scales in the local moment and specific heat of the half-filled two-dimensional Hubbard model, *Phys. Rev. B* **63**, 125116 (2001).
- [74] J. P. F. LeBlanc and E. Gull, Equation of state of the fermionic two-dimensional Hubbard model, *Phys. Rev. B* **88**, 155108 (2013).
- [75] T. Paiva, R. Scalettar, M. Randeria, and N. Trivedi, Fermions in 2D Optical Lattices: Temperature and Entropy Scales for Observing Antiferromagnetism and Superfluidity, *Phys. Rev. Lett.* **104**, 066406 (2010).
- [76] F. Werner, O. Parcollet, A. Georges, and S. R. Hassan, Interaction-Induced Adiabatic Cooling and Antiferromagnetism of Cold Fermions in Optical Lattices, *Phys. Rev. Lett.* **95**, 056401 (2005).
- [77] Z. Cai, H.-h. Hung, L. Wang, D. Zheng, and C. Wu, Pomeranchuk Cooling of $SU(2N)$ Ultracold Fermions in Optical Lattices, *Phys. Rev. Lett.* **110**, 220401 (2013).
- [78] Note that k is no longer a good quantum number under the open boundary condition, and thus there exist $k' \neq k$ s.t. $G(k, k', \beta/2) \neq 0$. Nevertheless, we find that the off-diagonal components are negligible, i.e., about 1% of total weights at $T = 2$ and 8% at $T = 1/3$.
- [79] W. Jiang, Y. Liu, A. Klein, Y. Wang, K. Sun, A. V. Chubukov, and Z. Y. Meng, Monte Carlo study of the pseudogap and superconductivity emerging from quantum magnetic fluctuations, *Nat. Commun.* **13**, 2655 (2022).
- [80] S. Lederer, Y. Schattner, E. Berg, and S. A. Kivelson, Superconductivity and non-Fermi liquid behavior near a nematic quantum critical point, *Proc. Natl. Acad. Sci. U.S.A.* **114**, 4905 (2017).
- [81] K.-S. Chen, Z. Y. Meng, T. Pruschke, J. Moreno, and M. Jarrell, Lifshitz transition in the two-dimensional Hubbard model, *Phys. Rev. B* **86**, 165136 (2012).
- [82] S. Sakai, Y. Motome, and M. Imada, Evolution of Electronic Structure of Doped Mott Insulators: Reconstruction of Poles and Zeros of Green's Function, *Phys. Rev. Lett.* **102**, 056404 (2009).
- [83] V. F. Maisi, S. V. Lotkhov, A. Kemppinen, A. Heimes, J. T. Muhonen, and J. P. Pekola, Excitation of Single Quasiparticles in a Small Superconducting Al Island Connected to Normal-Metal Leads by Tunnel Junctions, *Phys. Rev. Lett.* **111**, 147001 (2013).
- [84] N. Doiron-Leyraud, O. Cyr-Choinière, S. Badoux, A. Ataei, C. Collignon, A. Gourgout, S. Dufour-Beauséjour, F. F. Tafti, F. Laliberté, M. E. Boulanger, M. Matusiak, D. Graf, M. Kim, J. S. Zhou, N. Momono, T. Kurosawa, H. Takagi, and L. Taillefer, Pseudogap phase of cuprate superconductors confined by Fermi surface topology, *Nature Communications* **8**, 2044 (2017).
- [85] H.-C. Jiang and S. A. Kivelson, Stripe order enhanced superconductivity in the Hubbard model, *Proc. Natl. Acad. Sci. U.S.A.* **119**, e2109406119 (2022).
- [86] H. Xu, H. Shi, E. Vitali, M. Qin, and S. Zhang, Stripes and spin-density waves in the doped two-dimensional Hubbard model: Ground state phase diagram, *Phys. Rev. Res.* **4**, 013239 (2022).
- [87] C.-M. Chung, M. Qin, S. Zhang, U. Schollwöck, and S. R. White (The Simons Collaboration on the Many-Electron Problem), Plaquette versus ordinary d -wave pairing in the t' -Hubbard model on a width-4 cylinder, *Phys. Rev. B* **102**, 041106(R) (2020).
- [88] A. J. Dunnett and A. W. Chin, Efficient bond-adaptive approach for finite-temperature open quantum dynamics using the one-site time-dependent variational principle for matrix product states, *Phys. Rev. B* **104**, 214302 (2021).
- [89] J.-W. Li, A. Gleis, and J. von Delft, Time-dependent variational principle with controlled bond expansion for matrix product states, arXiv e-prints (2022), arXiv:2208.10972.
- [90] H. F. Trotter, On the product of semi-groups of operators, *Proc. Am. Math. Soc.* **10**, 545 (1959).
- [91] M. Suzuki, Relationship between d -dimensional quantal spin systems and $(d+1)$ -dimensional Ising systems—equivalence, critical exponents and systematic approximants of the partition function and spin correlations—, *Prog. Theor. Phys.* **56**, 1454 (1976).

Supplemental Material for Tangent Space Approach for Thermal Tensor Network Simulations of 2D Hubbard Model

I. Supplementary tanTRG Results

Below we show more benchmark results of the Hubbard model on the width $W = 4, 6$ cylinders, which turn out to be less challenging for tanTRG than the $W = 8$ case shown in Fig. 2 of the main text. In Sec. IA we show the simulated internal energy, specific heat, and entropy results, which turn out to be highly accurate. In Sec. IB we show topography analysis of the Matsubara Green's function $G(k, \beta/2)$ for the Hubbard models with next nearest neighboring (NNN) hopping $t'/t = 0$ and $t'/t < 0$. In Sec. IC the d -wave pairing responses vs various pinning fields h_p are shown. In Sec. ID we show the spin and charge correlations of $W = 4$ doped Hubbard model, which indicate a half-filled stripe phase. In Sec. IE we carefully analyze the typical errors of tanTRG at various temperatures.

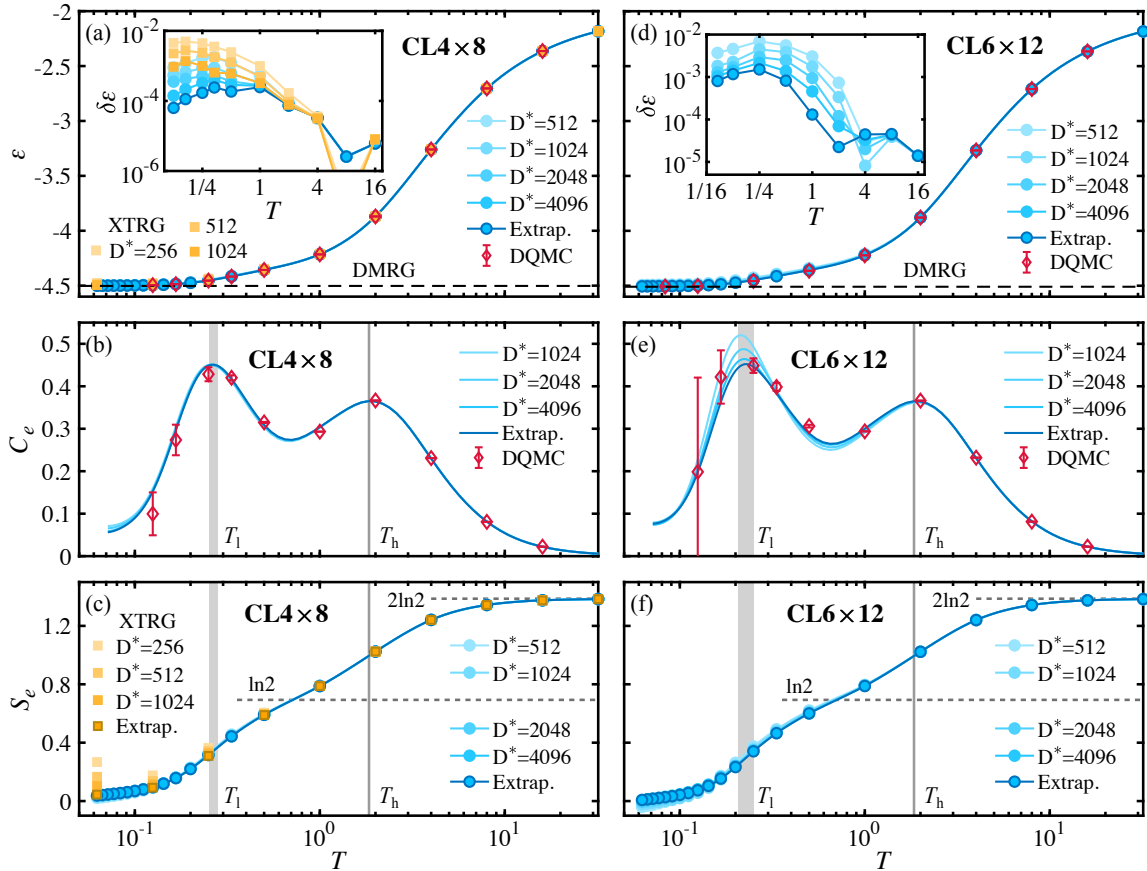


FIG. S1. Benchmark results on $W = 4$ and $W = 6$ cylinders. (a-c) show the energy ε , specific heat C_e , and entropy S_e of $CL4 \times 8$ lattice, and (d-f) show the corresponding results on the $CL6 \times 12$ lattice. The energy ε and specific heat C_e on both lattices show excellent agreements with DQMC calculations. For the $CL4 \times 8$ lattice, we also plot XTRG results of ε and S_e , with retained bond multiplets $D^* = 256, 512,$ and 1024 , whose extrapolation shows very good agreement with the tanTRG and DQMC results. In particular, the insets in (a,d) show the relative error of tanTRG results as compared to the standard DQMC data.

A. Benchmark of Hubbard cylinders at half-filling

In Fig. S1 we show the tanTRG results of the half-filled Hubbard model on $W = 4$ and $W = 6$ cylinder lattices, denoted as CL4 and CL6 henceforth. The on-site repulsive interaction is fixed as $U = 8$, and the results are compared to those obtained by determinant quantum Monte Carlo (DQMC) and exponential tensor renormalization group (XTRG) methods. In Fig. S1(a,d) we show the energy per site ε vs T with retained bond multiplets up to $D^* = 4096$, i.e., approximately $D = 25,000$ individual states,

with which we obtain highly accurate tanTRG results on both CL4 and CL6 lattices. The insets in Fig. S1(a,d) plot the relative errors of energy $\delta\varepsilon = |\varepsilon - \varepsilon_{\text{DQMC}}|/|\varepsilon_{\text{DQMC}}|$, which are of $O(10^{-4})$ for CL4 and $O(10^{-3})$ for CL6 till the lowest temperature $T/t \simeq 0.06$. Note they are already comparable to the estimated Trotter errors in practical DQMC calculations (c.f., Fig. S13 below). In Fig. S1(a) we also plot the XTRG results and show their relative errors $\delta\varepsilon$ in the inset of Fig. S1(a), from which we see that for the challenging Hubbard model and with the same retained bond dimension, the tanTRG can produce energy expectation values with higher accuracy than XTRG.

In Fig. S1(b,e), we show the tanTRG results of electron specific heat C_e on $W = 4$ and 6 cylinders, and see in both cases again two temperature scales. They are higher temperature scale $T_h/t \sim 2$ that corresponds to the charge degree of freedom and the lower temperature scale $T_l/t \sim 0.2$ for the spin degrees of freedom. The higher temperature scale T_h is found to be stable for different system sizes, while the lower scale T_l is slightly higher for the CL4 than those of CL6 and CL8. In Fig. S1(b,e) we also plot DQMC results of C_e and find excellent agreements within error bars for both geometries.

In Fig. S1(c), we show tanTRG and XTRG data of thermal entropy and find the accordant results decrease from the full entropy $\ln d$ ($d = 4$ is the dimension of local Hilbert space) and exhibit a two-step release at T_h and T_l , respectively. In the intermediate-temperature regime between the T_h and T_l , there exhibits a shoulder-like structure with a fractional entropy $\frac{1}{2} \ln d$. This can be ascribed to the fact that the two peaks, the higher charge peak and lower spin one. The former T_h corresponds to the appearance of local moments, and the antiferromagnetic spin correlations build up near the lower T_l scale. For the entropy calculations, we see again tanTRG can produce more accurate results than XTRG with the same bond dimension (and remember that tanTRG can retain much larger bond dimension up to $D^* = 4096$ vs 1024 for XTRG). In Fig. S1(f) we plot the tanTRG results of entropy data for CL6 case and also witness excellent convergence of S_e vs D^* .

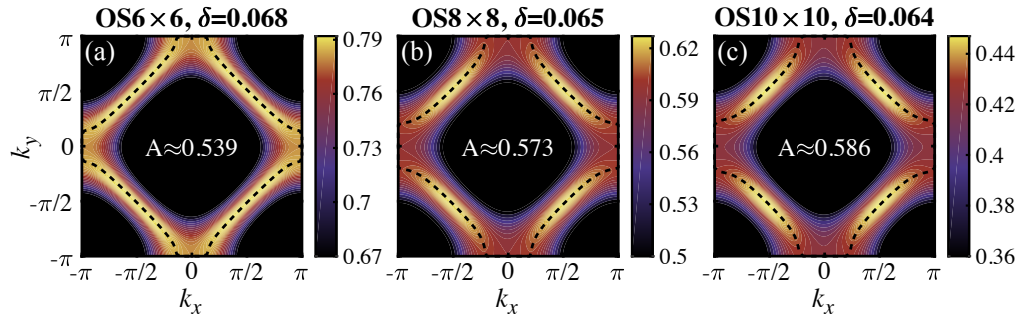


FIG. S2. (a-c) show the $\beta G(k, \beta/2)$ of doped Hubbard model on $L = 6, 8$ and 10 open square lattices with fixed $\mu = 2$ and $T = 1/3$. The OS6 \times 6 and OS8 \times 8 cases are computed with $D^* = 2048$ while OS10 \times 10 case with $D^* = 4096$.

B. Additional results of Matsubara Green's function

Now we show the Matsubara Green's function $\beta G(k, \beta/2)$ of t - t' Hubbard model

$$H = -t \sum_{\langle i,j \rangle, \sigma} (c_{i\sigma}^\dagger c_{j\sigma} + \text{H.c.}) - t' \sum_{\langle\langle i,j \rangle\rangle, \sigma} (c_{i\sigma}^\dagger c_{j\sigma} + \text{H.c.}) + U \sum_i n_{i\uparrow} n_{i\downarrow} - \mu \sum_i n_i, \quad (\text{S1})$$

where t' is the hopping between next nearest neighboring (NNN) sites $\langle\langle i, j \rangle\rangle$. We perform tanTRG calculations of the t - t' Hubbard model on square lattice with open boundary condition (OS). In Fig. S2, we compare the results on different system sizes, and find the Fermi surfaces become more holelike as the system sizes enlarge from OS6 \times 6 to OS10 \times 10. The node-antinode feature also becomes more distinguishable as system size increases.

For the OS8 \times 8 geometry, we further compare the results of $t'/t = 0$ [Fig. S3(a-d)] with those of $t'/t = -0.25$ [Fig. S3(e-h)]. In Fig. S3 we find the system with NNN hopping $t' < 0$ more favors the holelike Fermi surface, and the Lifshitz transition occurs at a clearly higher temperature than that of $t' = 0$ [c.f., Fig. S3(f) vs Fig. S3(c)]. More intriguingly, at a low temperature of $T/t = 1/3$ [Fig. S3(h)] we find a very prominent node-antinode structure in the $t'/t = -0.25$ case, which is also much more prominent than those of $t' = 0$ case shown in Fig. S3(d).

To see the Matsubara Green's function results more clearly, we show in Fig. S3(i,j) the results along the path indicated in the inset of Fig. S3(i) [i.e., $(0, 0) \rightarrow (\pi, 0) \rightarrow (\pi, \pi) \rightarrow (\pi/2, \pi/2) \rightarrow (0, 0)$]. At relatively high temperature, e.g., $T/t = 2$ and 1, we find similar intensities of spectral weight at $k = (\pi/2, \pi/2)$ and $k = (\pi, 0)$ points, for either $t'/t = 0$ [Fig. S3(i)] or $t'/t = -0.25$ [Fig. S3(j)]. However, as temperature further decreases to $T/t = 1/2, 1/3$, the difference in intensity between the $k = (\pi/2, \pi/2)$ and $k = (\pi, 0)$ points is visible for $t'/t = 0$ and becomes significant for $t'/t = -0.25$.

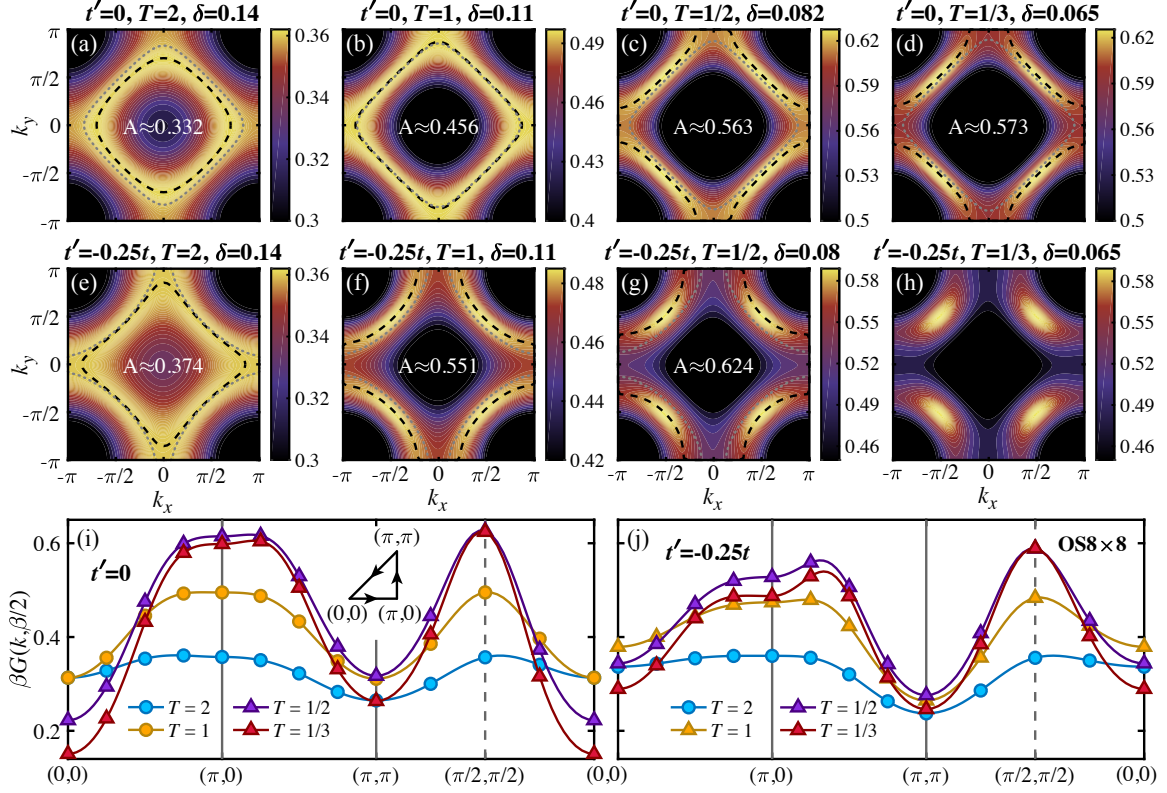


FIG. S3. (a-d) show the $\beta G(k, \beta/2)$ of OS8 \times 8 doped Hubbard model with NNN hopping $t' = 0$ and (e-h) for the case with $t'/t = -0.25$. The results are obtained with $D^* = 2048$, $U = 8$ and $\mu = 2$ on temperatures $T = 2, 1, 1/2$ and $1/3$. The doping levels vary with T are labeled in the corresponding plots. The black dashed lines label the maximal of $\beta G(k, \beta/2)$ and provide the estimated Fermi surfaces, where A denotes the area enclosed by the Fermi surface. The dotted lines denote the Fermi surfaces in the noninteracting limit. (i) and (j) plot the $\beta G(k, \beta/2)$ values along the path indicated in the inset of (i), for the $t' = 0$ and $t'/t = -0.25$ cases, respectively.

C. Pairing responses versus pairing fields

Now we show in Fig. S4 the computed results of pairing order parameter $\Delta_p = \frac{1}{N_p} \langle \Delta_{\text{tot}} \rangle_T$ (N_p the total bond number) under various pairing fields h_p . In Fig. 5 of the main text we have shown the pairing susceptibility $\chi_{\text{SC}} = \Delta_p/h_p$ with a small pinning field $h_p = 0.01$. Here in Fig. S4, we find the chosen $h_p = 0.01$ in the main text indeed well resides in the linear response regime, and the order parameter Δ_p vanishes as $h_p \rightarrow 0$, even for the lowest temperature $T/t = 1/24$. These observations thus validate that the pairing susceptibility χ_{SC} in Fig. 5 of the main text indeed reflects the intrinsic pairing responses of the system.

D. Spin and charge correlations for the $t' = 0$ Hubbard model

In Fig. S5 we show the tanTRG results of charge density distribution and spin-spin correlations. The results are computed on $\text{CL4} \times 24$ geometry with $U = 8$ and $\delta \approx 1/12$ controlled via a fine tuning of the chemical potential μ .

In Figs. S5(a-c) we show the electron density distributions on a width-4 cylinder. A charge stripe pattern is apparent at the lowest temperature $T = 1/48$ as visualized in Fig. S5(a), with its temperature evolution indicated in Fig. S5(b). The charge stripe can be already observed at $T = 1/24$, and becomes quite prominent for $T \leq 1/32$. This can also be clearly recognized in the Fourier transformation of electron density, ρ_k , shown in Fig. S5(c). From the results in Fig. S5(a-c), we observe a half-filled stripe with wave length $\lambda_{\text{CDW}} = 6 \approx 1/(2\delta)$ at sufficiently low temperature. Our calculations are consistent with previous results in Refs. [85, 86].

Regarding the spin-spin correlations, we also find a spin density wave (SDW) in Figs. S5(d-f). From a reference point in the bulk [labeled by a cross in Fig. S5(d)], we find the correlation $(-1)^{r_x+r_y} S(r_x, r_y)$ changes its sign every 6 sites along the length direction, i.e., a π -phase shift occurs for $\lambda_{\text{SDW}}/2 = 6$ that equals λ_{CDW} . Besides, as temperature lowers the spin-spin correlation strengthens [see Fig. S5(e)] and the structure factors exhibit peaks at $k_x = (1 \pm 2\delta)\pi$ [Fig. S5(f)]. Our findings are consistent with

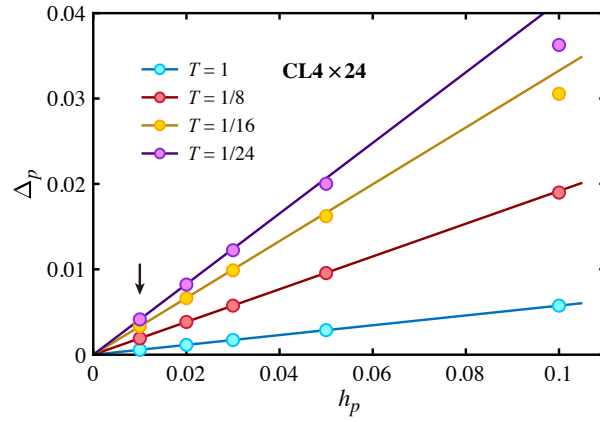


FIG. S4. The d -wave pairing order parameter Δ_p of the $\text{CL4} \times 24$ Hubbard model with different pairing fields $0.01 \leq h_p \leq 0.1$. The results are computed for the $\mu = 1.75$ case, with $D^* = 1024$ bond multiplets retained. The solid lines connect the origin and data point $h_p = 0.01$, and extrapolate to the larger h_p regime, from which we find the data points with $h_p \leq 0.05$ well fall into a linear response regime.

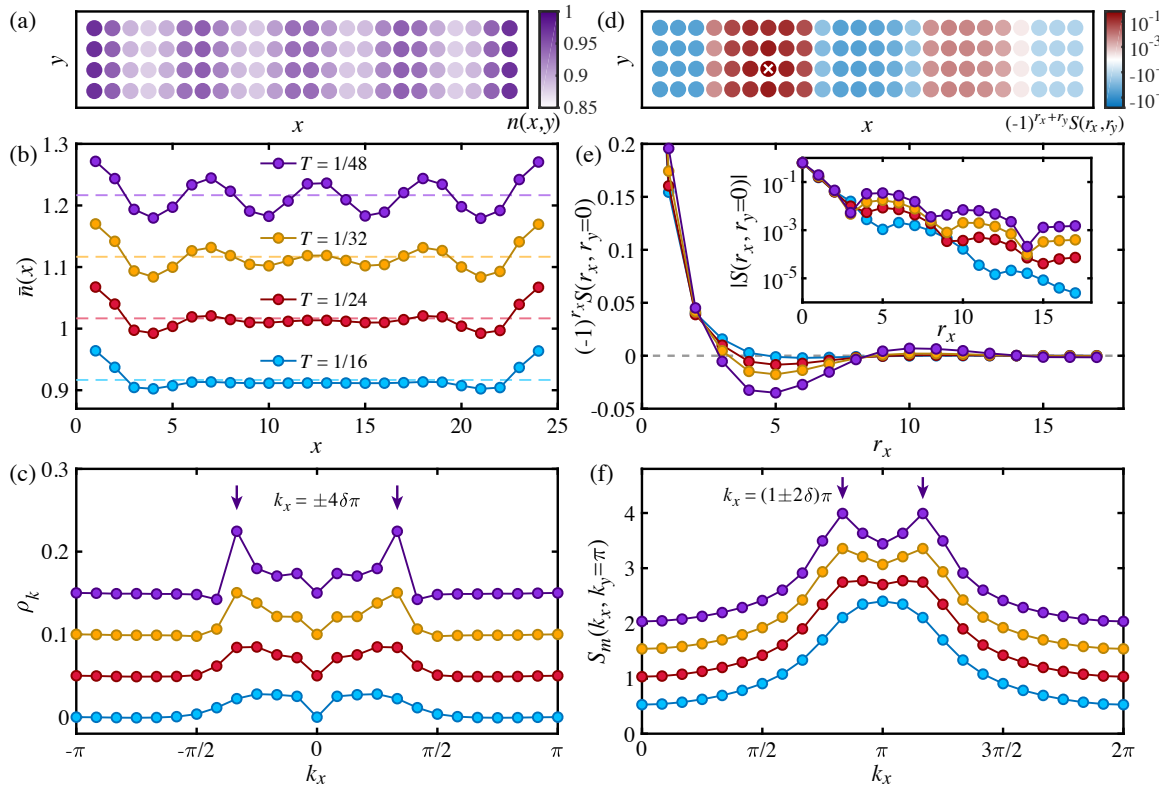


FIG. S5. (a) shows the electron density $n(x, y)$ computed at low temperature $T = 1/48$, where the charge stripe can be observed clearly. (b) shows the electron density $\bar{n}(x) = \frac{1}{W} \sum_{y=1}^W n(x, y)$ at various temperatures ($W = 4$ denotes the width of the cylinder), where the dashed lines denote the average electron density $\bar{n} = 1 - \delta$. (c) shows the Fourier transformation $\rho_k = \frac{1}{\sqrt{L}} \sum_{x=1}^L e^{-ik_x x} (\bar{n}(x) - \bar{n})$, where $L = 24$ is the length of cylinder, and the double peaks located at $k_x = \pm 4\delta\pi$ clearly indicate the presence of (half-filled) charge stripe in the system. (d) shows the spin correlation $(-1)^{r_x+r_y} S(r_x, r_y) = (-1)^{r_x+r_y} \langle S_{x,y} \cdot S_{x+r_x, y+r_y} \rangle$ at $T = 1/48$, observed from the reference point labeled by a cross. (e) shows the spin correlations along the length direction, where the periodically appearing “nodes” in $(-1)^{r_x+r_y} S(r_x, r_y)$ (and “dips” in the absolute value $|S(r_x, r_y = 0)|$ in the inset) correspond to the sign change (π -phase shift) in the short-range SDW. (f) shows the spin structure factor $S_m(k) = \frac{1}{LW} \sum_{i,j} e^{-ik(r_j-r_i)} \langle S_i \cdot S_j \rangle$, where the peaks located at $k_x = (1 \pm 2\delta)\pi$ are consistent with SDW observed on panel (d). Note that the curves in panel (b,c,f) are each shifted upwards by, $\Delta\bar{n} = 0.1$, $\Delta\rho_k = 0.05$, and $\Delta S_m = 0.5$, for the charge density, its Fourier transformation, and spin structure factor results, respectively, for the sake of clarity. All the above results are obtained with tanTRG by retaining $D^* = 2048$ [about 5500 equivalent $U(1)$ states] and with a fine tuned chemical potential $\mu \approx 1.8$ in the temperature range of interest.

the $W = 4$ results reported in Refs. [86] and [21].

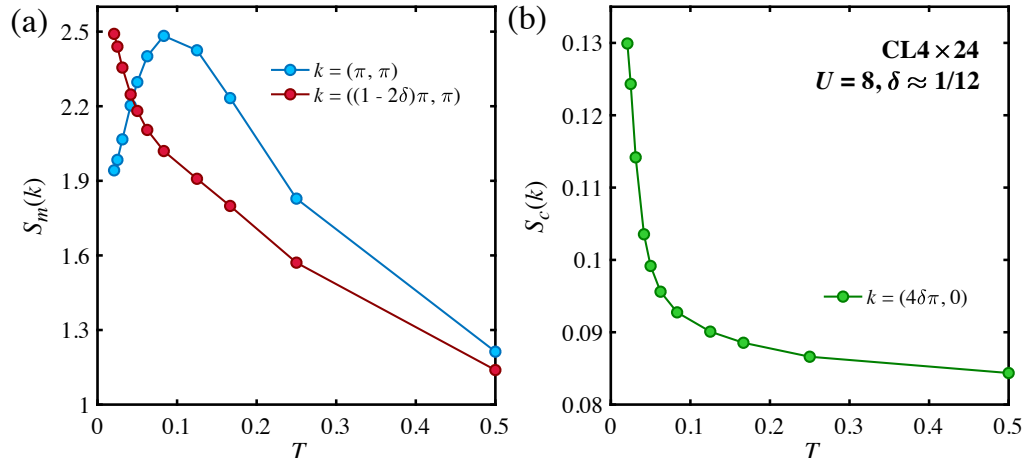


FIG. S6. (a,b) show the tanTRG results on $CL4 \times 24$ lattice, with $U = 8$ and approximately fixed doping $\delta \approx 1/12$ (controlled by fine tuning μ in the grand canonical ensemble simulations). The tanTRG results are obtained with $D^* = 2048$ [about 5500 equivalent $U(1)$ states].

In Fig. S5 we have already shown the results of half-filled stripe obtained on the width-4 cylinder that are in agreement with the minimally entangled typical thermal states (METTS) results [17]. In Fig. S6, we further show that the spin and charge structure factors obtained by tanTRG exhibit similar behaviors to METTS results, though with different on-site interactions and dopings, i.e., $U = 8$ and $\delta \approx 1/12$ in tanTRG vs $U = 10$ and $\delta = 1/16$ in METTS. The presence of a hump in $S_m(\pi, \pi)$ at intermediate temperature and the ever increasing $S_m((1 - 2\delta)\pi, \pi)$ curve with a shoulder structure are reproduced in our tanTRG calculations. On the other hand, the charge structure factor at $k = (4\delta\pi, 0)$ increases rapidly as temperature decreases [c.f., Fig. S6(b)], also in qualitative agreement with METTS.

Last, it is worthwhile discussing the advantages and disadvantages of the two methods, tanTRG and METTS. They represent two typical tensor-network approaches, MPO-based (purification) vs MPS-based (with Monte Carlo samplings), for finite temperature simulations. Unlike current METTS calculations that use Trotter decomposition and swap gates (at least initially) and require separate runs for each temperature point, tanTRG generates all temperature points in one run and is free of statistical errors. It is straightforward to implement Abelian and non-Abelian symmetries in tanTRG, which further improves its efficiency and enables wider systems (width-8 vs width-4 cylinders) to be calculated. As the MPO representation of density operator is available, it is more convenient to compute certain quantities like the imaginary-time correlations, pairing susceptibilities, etc, in tanTRG. On the other hand, METTS works with the canonical ensemble, and thus it is easier to control the particle number in the calculations. Moreover, METTS is well suited for multi-core parallel computing as it uses Monte Carlo samplings in its calculations.

E. Error analysis of tanTRG

In tanTRG, there exist different types of errors. The majors are three, expansion error in the initialization, Lie-Trotter error, and the projection error. In Fig. 1(c) of the main text, we observed two dips, i.e., cancellation points that naturally separates three regimes where the three types of errors dominate. In the high-temperature regime, the 1st-order expansion $\rho_0 = 1 - \tau_0 H$ is the main resource of error, which can be suppressed by the Taylor expansion to higher order, namely, $\rho_0 = \sum_{n=0}^{N_c} \frac{(-\tau_0 H)^n}{n!}$ expanded up to a sufficiently large N_c , with the techniques developed in series-expansion thermal tensor network (SETTN) approach [65]. As shown in Fig. S7(a), the relative error δF for $\beta \lesssim 10^{-2}$ can be suppressed to machine precision, i.e., $\sim 10^{-15}$ with the SETTN initialization.

In the intermediate-temperature regime marked by blue color in Fig. S7(a,b), the Lie-Trotter splitting becomes the main source of computational errors. In Fig. S7(b), we find the Lie-Trotter errors in this intermediate regime decrease as step length τ is reduced. Since that the sign of Lie-Trotter errors turns out to be different with expansion error, there exists a cancellation point at $\beta \sim 10^{-2}$ (i.e., a dip). Note that the location of this first dip can be pushed to high-temperature side when SETTN technique is used in the initialization [c.f., Fig. S7(a) where the cancellation point becomes virtually invisible due to the negligible expansion error with SETTN initialization].

Finally, at low temperature $\beta \gtrsim 1$ the 1-site projection errors, which reflect the expression capability of MPO representation

with given bond dimension D , become sufficiently large and dominate over all other type of errors after the second dip.

In Fig. S7(c) we show the scaling analysis of Lie-Trotter error at a fixed (inverse) temperature $\beta = 9$, where the relative errors $\delta F_{\text{Lie-Trotter}}$ are found to scale as $c\tau^\alpha$ with $\alpha \approx 2$. The fitted prefactor c is plotted in the inset, from which we find the prefactor, and thus the overall Lie-Trotter errors, can be well controlled by the bond dimension D . This surprising finding is in stark difference to the Trotter-Suzuki decomposition errors in other thermal TN methods, where the Trotter error is independent of retained MPO bond dimension [30].

Moreover, the 2-site projection errors in the initial stage of MPO cooling, which is sometimes problematic for MPS-based TDVP calculations (e.g., when starting from a direct product state), are largely absent in tanTRG. A possible reason is that the additional physical indices in MPO introduce more variational parameters, bearing some similarity to the role of subspace expansion in MPS for mitigating the large initial 2-site projection errors [59, 88].

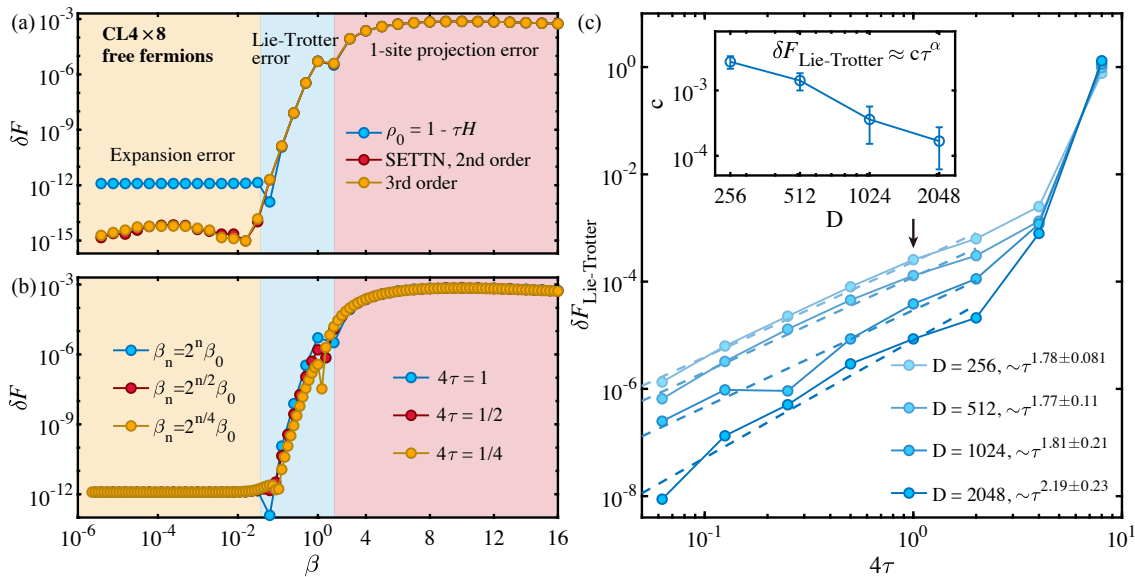


FIG. S7. Relative errors in free energy of $\text{CL4} \times 8$ free fermions. (a) The SETTN initialization reduces the expansion error at high temperatures down to the machine precision. (b) compares the Lie-Trotter errors with different temperature grids, more specifically $\beta_n = 2^n \beta_0$, $2^{n/2} \beta_0$, and $2^{n/4} \beta_0$ used in exponential cooling and $4\tau = 1, 1/2$ and $1/4$ in the linear cooling. The errors curves of different grids coincide, except for in the intermediate-temperature regime. Moreover, when decreasing the step length, the second (lower- T) cancellation point moves towards higher temperature since the Lie-Trotter error decreases while the 1-site projection error is independent on step length. Both (a) and (b) are computed by tanTRG with a fixed $D = 1024$. (c) estimates the Lie-Trotter errors by $\delta F_{\text{Lie-Trotter}} = |F - F_0|/|F_0|$ at a fixed (inverse) temperature $\beta = 9$. In particular, F_0 is also obtain by tanTRG with a sufficiently small $\tau = 1/128$, and all calculations are evolved from the same density operator $\rho(\beta \equiv 1)$. $\delta F_{\text{Lie-Trotter}}$ results are found fall into a $c\tau^\alpha$ behavior with $\alpha \approx 2$ and the prefactor c controlled by D as shown in the inset. The black arrow denotes the step length we used throughout in the main text, which corresponds to negligible Lie-Trotter error as compared to the dominant 1-site projection error.

II. Derivation of Tangent Space Approach for Thermal Tensor Networks

Here we provide details in deriving the flow equation of density operator ρ in the imaginary-time evolution, as well as technical details of the algorithms involved in the main text. For the sake of simplicity, we firstly introduce the Choi transformation that maps the matrix product operator (MPO) ρ to a matrix product state (MPS) $|\rho\rangle\rangle$ in Sec. II A, which thus allows us to follow the standard derivation of time dependent variational principle (TDVP) approach [56, 58], with some adaptation to the super MPS mapped from MPO. We present a short introduction to the MPS manifold and tangent vectors in Sec. II B, and the orthogonal condition [57, 60] in Sec. II C. After that, we derive the flow equation induced by the optimal tangent vectors in Sec. II D, and then introduce the splitting method for integration together with the Lie-Trotter error analysis in Sec. II E. The single-site 1-TDVP integrator is detailed in Sec. II F, and two-site 2-TDVP in Sec. II G. The latter allows the bond dimension to increase and is very useful in the imaginary-time evolution of ρ . Another useful technique, Lanczos exponential method used for updating local tensors, is present in Sec. II H. Lastly, bearing in mind that the super MPS language, essentially equivalent to MPO representation, is introduced here merely to facilitates the derivatives of flow equation in the main text.

A. Choi transformation

We denote the Hilbert space as \mathcal{H} and the space of bounded linear operators on \mathcal{H} as $B(\mathcal{H})$, and the Choi transformation is defined as follows

$$B(\mathcal{H}) \rightarrow \mathcal{H} \otimes \mathcal{H}$$

$$\rho = \sum_{ij} \rho_{ij} |i\rangle \langle j| \mapsto |\rho\rangle\rangle \equiv \sum_{ij} \rho_{ij} |i\rangle \otimes |j\rangle, \quad (\text{S2})$$

which represents an isomorphism between Hilbert spaces. Note that the Choi transformation depends on the specific basis $\{|i\rangle\}$ that we choose. In particular, an MPO can be mapped into a (super) MPS via the Choi transformation as shown in Fig. S8(a). Meanwhile, for a linear super operator \mathcal{L} acting on ρ , represented as $\rho \mapsto A\rho B$, the Choi transformation is as follows

$$\mathcal{L}\rho = A\rho B \mapsto A \otimes B^T |\rho\rangle\rangle, \quad (\text{S3})$$

which satisfies the commutative diagram

$$\begin{array}{ccc} B(\mathcal{H}) & \xrightarrow{\text{Choi}} & \mathcal{H} \otimes \mathcal{H} \\ \mathcal{L} \downarrow & & \downarrow A \otimes B^T \\ B(\mathcal{H}) & \xrightarrow{\text{Choi}} & \mathcal{H} \otimes \mathcal{H}. \end{array} \quad (\text{S4})$$

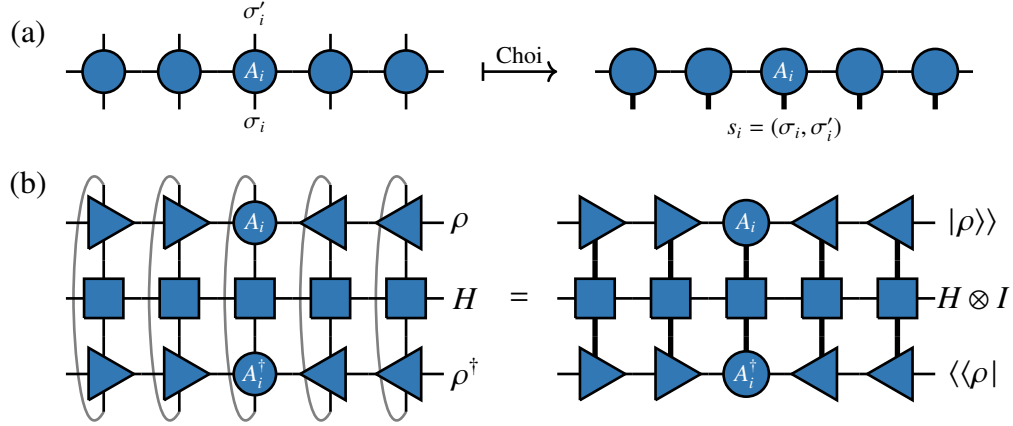


FIG. S8. (a) shows the mapping between MPO and (super) MPS via the Choi transformation. Note that we set the physical index a *bold* line to emphasize that it is a combined index $s_i \equiv (\sigma_i, \sigma'_i)$. (b) depicts the equivalence between the tensor network representations of $\text{Tr}\{\rho^\dagger H \rho\}$ (left) and $\langle\langle \rho | H \otimes I | \rho \rangle\rangle$ (right). By substituting the rank-4 tensor A_i in MPO with rank-3 local tensor A_i (with a bold index) in MPS, we arrive at the right-hand-side of the equation. Note the identity I at the right-hand-side of the equation will be skipped henceforth for the sake of simplicity.

With this transformation, we map the imaginary-time evolution equation $d\rho/d\beta = -H\rho$ to an equation of state, i.e.,

$$\frac{d}{d\beta} |\rho\rangle\rangle = -H \otimes I |\rho\rangle\rangle. \quad (\text{S5})$$

Although in principle we need to evolve the super MPS $|\rho\rangle\rangle$ according to the super operator $H \otimes I$, it can be simplified by taking virtual of the fact $e^{H \otimes I} = e^H \otimes I$, i.e., the identity operator I acting on one-half of physical indices is trivial and can thus be safely neglected.

To obtain the expectation values, we need to compute the trace with density operators, which can be represented as an inner product of super MPS, e.g., the energy expectation can be computed as

$$E(\beta) = \frac{\text{Tr}\{\rho^\dagger(\beta/2) H \rho(\beta/2)\}}{\text{Tr}\{\rho^\dagger(\beta/2) \rho(\beta/2)\}} = \frac{\langle\langle \rho(\beta/2) | H \otimes I | \rho(\beta/2) \rangle\rangle}{\langle\langle \rho(\beta/2) | \rho(\beta/2) \rangle\rangle}, \quad (\text{S6})$$

with the corresponding tensor network representations shown in Fig. S8(b). Note we have used a bilayer trick in the Gibbs operator representation [67], i.e., $\rho(\beta) = \rho(\beta/2) \rho^\dagger(\beta/2)$.

The second \mathcal{H} of the Hilbert space $\mathcal{H} \otimes \mathcal{H}$ is an auxiliary system (B), and thus the partial trace gives the density matrix of the physical system (A)

$$\begin{aligned} \text{Tr}_B |\rho(\beta/2)\rangle\rangle \langle\langle \rho(\beta/2) | &= \sum_{ijkl} \rho_{ij} \rho_{kl}^* \text{Tr}_B |i\rangle_A |j\rangle_B \langle k|_A \langle l|_B = \sum_{ijkl} \rho_{ij} \rho_{kl}^* \delta_{jl} |i\rangle_A \langle k|_A \\ &= \sum_{ijk} \rho_{ij} \rho_{kj}^* |i\rangle_A \langle k|_A = \sum_{ik} \left(\rho(\beta/2) \rho^\dagger(\beta/2) \right)_{ik} |i\rangle_A \langle k|_A \\ &= \rho(\beta/2) \rho^\dagger(\beta/2) = \rho(\beta), \end{aligned} \quad (\text{S7})$$

which means the supervector $|\rho(\beta/2)\rangle\rangle$ actually represents a purification of the Gibbs operator $\rho(\beta)$.

B. MPS/MPO manifold and gauge redundancy

Through the Choi transformation, we can map the MPO to a super MPS. The latter can generically be represented as

$$|\Psi(A)\rangle\rangle = \sum_{\{s_i\}} \text{Tr} \left\{ A_1^{s_1} \cdots A_N^{s_N} \right\} |s_1 \cdots s_N\rangle, \quad (\text{S8})$$

where each A_i is a rank-3 tensor with a bold physical index $s_i = 1, \dots, \tilde{d}_i$, with $\tilde{d}_i = d_i^2$, dimension of local Hilbert space squared and two bond indices running over $1, \dots, D_{i-1}$ and $1, \dots, D_i$, for $(i-1)$ -th and i -th bonds, respectively.

$$A = (A_1, \dots, A_N) \in \bigoplus_{i=1}^N \mathbb{C}^{D_{i-1} D_i \tilde{d}_i} \equiv \mathbb{A} \quad (\text{S9})$$

denotes the parameters of MPS. An MPS is full-rank if there are exactly D_i non-zero singular values for each bond. A subset comprised of all full-rank MPSs in \mathbb{A} forms a manifold \mathcal{A} . Note that the MPS representation always has gauge redundancy, i.e., two MPSs may be essentially equivalent up to a gauge transformation

$$A_i^{s_i} \mapsto G_{i-1}^{-1} A_i^{s_i} G_i, \quad (\text{S10})$$

where $(G_1, \dots, G_{N-1}) \in \mathcal{G} = \prod_{i=1}^{N-1} \text{GL}(D_i, \mathbb{C})$ is the gauge group acting on the bond space and $G_0 = G_N \equiv 1 \in \text{GL}(1, \mathbb{C})$ specially. With this gauge group action, \mathcal{A} forms a principal bundle with base manifold $\mathcal{M} = \mathcal{A}/\mathcal{G}$, and \mathcal{M} is right the MPS manifold, a regular submanifold embedding to the Hilbert space \mathcal{H} .

To (partially) fix the gauge, one can introduce the canonical form of MPS. For example, the canonical condition of local tensor A_i reads

$$\begin{cases} \sum_{s_i} A_i^{s_i \dagger} A_i^{s_i} = c I_{D_i}, & \text{(left)} \\ \sum_{s_i} A_i^{s_i} A_i^{s_i \dagger} = c I_{D_{i-1}}, & \text{(right)} \end{cases} \quad (\text{S11})$$

where c is a constant normalization factor and I_{D_i} the $D_i \times D_i$ identity matrix. One can gauge the local tensors to left- or right-canonical form, denoted as A^L or A^R respectively. Below we take the gauge convention of MPS as follows: it has a site called canonical center, where all the local tensors on its left are left-canonical and right-canonical on the right.

C. Tangent vectors of MPS manifold

A tangent vector on the manifold forms like a summation of N MPSs with the i -th local tensor A_i varied, as observed by

$$\frac{d}{dt} |\Psi(A)\rangle\rangle = \sum_{i=1}^N \frac{\partial |\Psi(A)\rangle\rangle}{\partial A_i} \cdot \frac{dA_i}{dt} = \sum_{i=1}^N \sum_{\{s_j\}} \text{Tr} \left\{ A_1^{s_1} \cdots A_{i-1}^{s_{i-1}} \frac{dA_i^{s_i}}{dt} A_{i+1}^{s_{i+1}} \cdots A_N^{s_N} \right\} |s_1 \cdots s_N\rangle. \quad (\text{S12})$$

Following the mixed gauge convention of the MPS tangent vectors, we place each varied tensor at the canonical center of the MPS, and arrive at a surjective tangent map $\Phi : T\mathcal{A} \rightarrow T\mathcal{M}$, i.e.,

$$|\Phi_A(B)\rangle\rangle = \sum_{i=1}^N |\Phi_A^i(B_i)\rangle\rangle = \sum_{i=1}^N \sum_{\{s_j\}} \text{Tr} \left\{ (A^L)_1^{s_1} \cdots (A^L)_{i-1}^{s_{i-1}} B_i^{s_i} (A^R)_{i+1}^{s_{i+1}} \cdots (A^R)_N^{s_N} \right\} |s_1 \cdots s_N\rangle, \quad (\text{S13})$$

where the tangent bundle $T\mathcal{A}$ is parameterized as $(A, B) = (A_1, \dots, A_N, B_1, \dots, B_N)$. According to this tangent map, any flow equation

$$\frac{d}{dt} |\Psi(A)\rangle = |\Phi_A(B)\rangle \in T_{|\Psi(A)\rangle} \mathcal{M} \quad (\text{S14})$$

on the MPS manifold can be pulled back to the flow equation $dA/dt = B$ in the parameter space. Note that flow equation Eq. (S14) describes the evolution of state $|\Phi_A(B)\rangle$, and we need the flow equation for the local tensors that is convenient to deal with in the algorithmic level.

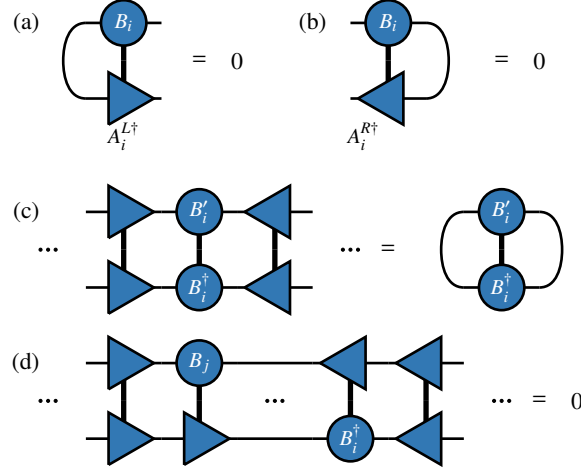


FIG. S9. (a, b) show the left and right orthogonal conditions, respectively. (c) illustrates that the pullback inner product between two local tensors on the same site is just the standard Euclidean inner product of the local tensors. (d) shows that the inner product between two different sites vanishes because of the orthogonal gauge fixing condition.

In the MPS representation of tangent vectors, there also exists gauge redundancy in tangent space that needs to be fixed. Here we adopt the orthogonal condition

$$\begin{cases} \sum_{s_i} A_i^{s_i \dagger} B_i^{s_i} = 0, & (\text{left}) \\ \sum_{s_i} B_i^{s_i} A_i^{s_i \dagger} = 0, & (\text{right}) \end{cases} \quad (\text{S15})$$

to fix the gauge and facilitate the optimization process later. This is shown in Fig. S9(a-b). With this we find

$$\langle \Phi_A^i(B_i) | \Phi_A^j(B_j') \rangle = \delta_{ij} \sum_{s_i} \text{Tr} \{ B_i^{\dagger s_i} B_i'^{s_i} \} = \delta_{ij} \langle B_i, B_i' \rangle, \quad (\text{S16})$$

i.e., the pullback inner product in parameter space $T_A \mathcal{A} \simeq \bigoplus_{i=1}^N \mathbb{C}^{D_{i-1} D_i \tilde{d}_i}$ is nothing but the standard Euclidean one, as illustrated in Fig. S9(c-d). At the same site it is just a full contraction of two local tensors that results in a scalar; on the contrary, at different sites the inner product simply vanishes.

D. Optimization of tangent vector within the tangent space

Let $|X_A\rangle \in T_{|\Psi(A)\rangle} \mathcal{H}$ be any tangent vector in the Hilbert space, its local component projected onto the tangent space and on the i -th site can be defined as

$$X_i = \frac{\partial}{\partial B_i^\dagger} \langle \Phi_A^i(B_i) | X_A \rangle \quad (\text{S17})$$

shown in Fig. S10(a), where $\langle \Phi_A^i(B_i) | X_A \rangle = \langle B_i, X_i \rangle$ under the mixed gauge condition. The optimization problem amounts to minimize the distance

$$\|\Phi_A(B) - X_A\|^2 = \sum_i (\langle B_i, B_i \rangle - \langle B_i, X_i \rangle - \langle X_i, B_i \rangle) + \|X_A\|^2. \quad (\text{S18})$$

Without loss of generality, we choose the left-orthogonal condition in the tangent space [c.f., Fig. S9(a)] and optimize the parameter B_i to minimize the Lagrangian

$$\mathcal{L} = \langle B_i, B_i \rangle - \langle B_i, X_i \rangle - \langle X_i, B_i \rangle + \sum_{\alpha\beta} \lambda_{\alpha\beta} \sum_{s_i, \gamma} \overline{(B_i)_{\gamma\alpha}^{s_i}} (A_i^L)_{\gamma\beta}^{s_i}, \quad (\text{S19})$$

where $\lambda_{\alpha\beta}$'s denote the D_i^2 multipliers imposing the left-orthogonal condition. The solution of this conditional extremum problem is

$$(B_i)_{\alpha\beta}^{s_i} = (X_i)_{\alpha\beta}^{s_i} - \sum_{s'_i, \gamma, \delta} \overline{(A_i^L)_{\delta\gamma}^{s'_i}} (X_i)_{\delta\beta}^{s'_i} (A_i^L)_{\alpha\gamma}^{s_i}, \quad (\text{S20})$$

as illustrated in Fig. S10(b). Note that left-orthogonal condition can only be imposed to the left $N - 1$ sites, and on the last site N Eq. (S20) reduces to $(B_N)_{\alpha\beta}^{s_N} = (X_N)_{\alpha\beta}^{s_N}$.

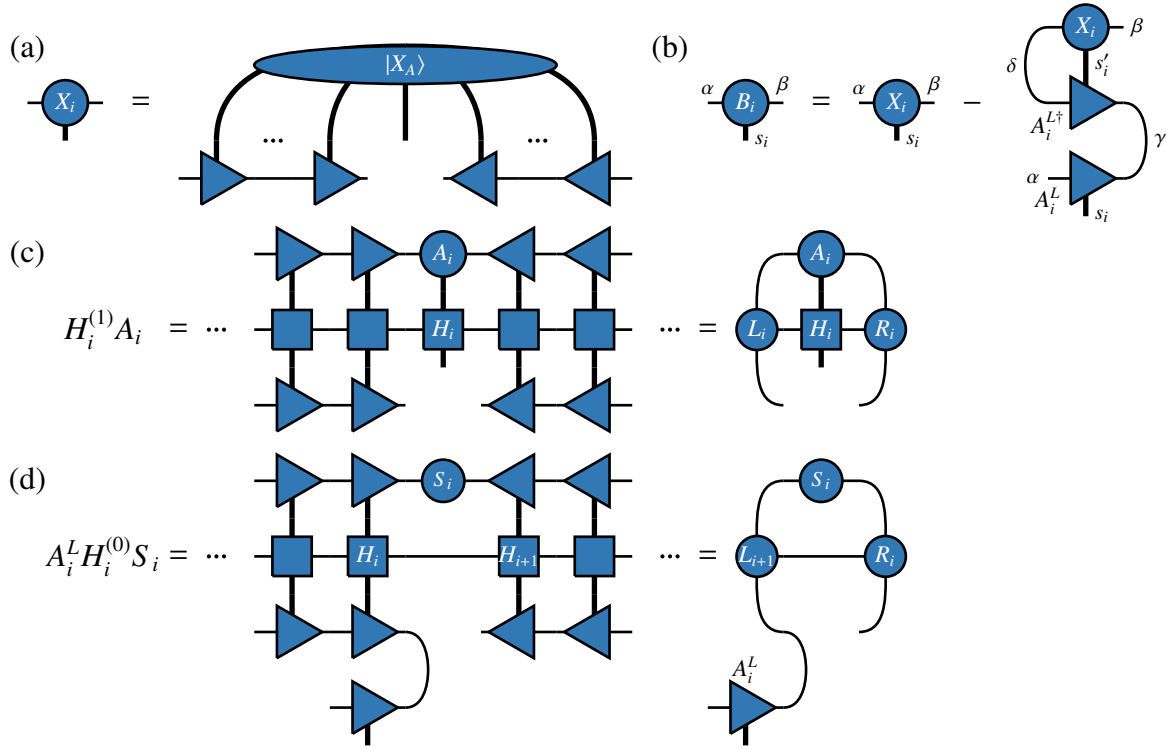


FIG. S10. (a) shows the definition of local component X_i of a tangent vector $|X_A\rangle$. (b) shows the tensor network representation of optimal tensor parameter B_i . (c) shows the local component $X_i = H_i^{(1)} A_i$ for the tangent vector $|X_A\rangle = H|\Psi(A)\rangle$, where L_i and R_i are the rank-3 left and right environment tensors of the i -th site, respectively. Substitute X_i in the second term of (b), and decompose $A_i = A_i^L S_i$, we arrive at the tensor structure in (d), which represents $A_i^L H_i^{(0)} S_i$.

In the present problem of interest, the tangent vector is generated by $|X_A\rangle = -H|\Psi(A)\rangle$, and the first term X_i in Eq. (S20) is a result of 1-site effective Hamiltonian $H_i^{(1)}$ acting on the local tensor A_i , i.e., $-H_i^{(1)} A_i$ [c.f., Fig. S10(c)]. Regarding the second term in Eq. (S20), we firstly take a tensor decomposition $A_i = A_i^L S_i$ via, e.g., the QR decomposition, to move the MPS from a site canonical form to a bond canonical one. The second term of Eq. (S20) thus becomes $A_i^L H_i^{(0)} S_i$, where $H_i^{(0)}$ denotes the bond effective Hamiltonian [c.f., Fig. S10(d)]. Therefore, pulled back via the tangent map (S13), the flow equation of local tensor A_i reads

$$\frac{dA_i}{d\beta} = -H_i^{(1)} A_i + A_i^L H_i^{(0)} S_i, \quad (\text{S21})$$

which is right the Eq. (2) of the main text, whose integration generates the required solution $A_i(\beta)$.

E. Splitting method and Lie-Trotter errors

Substituting Eq. (S21) into the tangent map Eq. (S13), the optimal tangent vector reads

$$\frac{d}{d\beta} |\Psi(A)\rangle = \sum_{i=1}^N |\Phi_A^i(-H_i^{(1)} A_i)\rangle + \sum_{i=1}^{N-1} |\Phi_A^i(A_i^L H_i^{(0)} S_i)\rangle, \quad (\text{S22})$$

reemphasize that the left(right)-orthogonal condition is imposed on each site but the last(first) one. Each term of this summation constitutes a linear equation as $H_i^{(1)}$ ($H_i^{(0)}$) independent on A_i (S_i), while the combination as a whole is nonlinear. A standard technique to integrate it is the splitting method [61], i.e., we split the tangent vector field corresponding to Eq. (S22) into the $2N - 1$ tangent vector fields, and arrive at the following linear equations

$$\frac{d}{d\beta} |\Psi(A)\rangle = |\Phi_A^i(-H_i^{(1)} A_i)\rangle \quad \text{and} \quad \frac{d}{d\beta} |\Psi(A)\rangle = |\Phi_A^i(A_i^L H_i^{(0)} S_i)\rangle \quad (\text{S23})$$

that can be successively integrated one by one. With tensor-network parameterization, the linear equations of local tensors read

$$\frac{dA_i}{d\beta} = -H_i^{(1)} A_i \quad \text{and} \quad \frac{dS_i}{d\beta} = H_i^{(0)} S_i, \quad (\text{S24})$$

which can be exactly solved as $A_i(\beta + \tau) = e^{-\tau H_i^{(1)}} A_i(\beta)$ and $S_i(\beta + \tau) = e^{\tau H_i^{(0)}} S_i(\beta)$. Generically, such a splitting leads to Lie-Trotter errors that scale as $O(\tau)$, which, however, can be reduced to $O(\tau^2)$ when we choose a symmetric integrator, i.e., composition of left-to-right and right-to-left sweeps that are adjoint with each other [58, 61, 89].

Moreover, when restricted to the affine Hilbert space $T_{|\Psi(A)\rangle} \mathcal{M}$, instead of the MPS manifold \mathcal{M} , the flow equation as a whole is guaranteed to be linear. After the same splitting procedure, and given the orthogonal conditions, it resorts to solving the system consisted of $2N - 1$ effective Hamiltonians that are mutually commutative, and the Lie-Trotter splitting becomes exact in this case. Back to the standard 1-TDVP on manifold \mathcal{M} , we argue that the Lie-Trotter error decreases as the bond dimension D is increased, as the manifold \mathcal{M} locally resembles the tangent space $T_{|\Psi(A)\rangle} \mathcal{M}$ in the large D limit. Therefore, the Lie-Trotter error, as well as the projection error, is well controlled by the parameter D , and this constitutes a very promising feature of tangent-space based approach of tensor networks.

F. Procedure of 1-TDVP

We describe the comprehensive procedure of 1-TDVP integrator, adapted for the imaginary-time evolution of super MPS $|\rho\rangle\rangle$, in the practical level as follows.

1. Starting from the leftmost site, i.e. $i = 1$, which is also the canonical center of the super MPS, with the left-orthogonal condition of tangent vector [Fig. S9(a)] is considered.
2. Integrate the first term of Eq. (S21) and obtain $A(\beta_0 + \tau) = e^{-H_i^{(1)} \tau} A_i(\beta_0)$, where τ is the step length.
3. Take a decomposition $A_i = A_i^L S_i$ via the QR or singular value decomposition (SVD), and gauge the super MPS $|\rho\rangle\rangle$ to a bond canonical form centered at i -th bond.
4. Integrate the second term of Eq. (S21) and update the bond tensor $S_i(\beta_0 + \tau) = e^{H_i^{(0)} \tau} S_i(\beta_0)$.
5. Contract the updated bond tensor $S_i(\beta_0 + \tau)$ with the local tensor A_{i+1}^R to the right of bond i , thus moving the canonical center to site $i + 1$.
6. Repeat steps 2-5 until the canonical center arrives at the rightmost site N , where no bond update is needed to the right of this site.
7. Sweep backwards from right to left, following the same line as the forward sweep and with the right-orthogonal condition [Fig. S9(b)] imposed instead.

G. 2-TDVP in the initial stage

As the imaginary-time evolution of MPO ρ (or equivalently the super MPS $|\rho\rangle\rangle$) starts from a high-temperature initial state $\rho(\tau_0) = 1 - \tau_0 H$ whose bond dimension is relatively small, as $D = D_H$ (bond dimension of the Hamiltonian MPO). It is therefore necessary to devise an algorithm that can increase the bond dimension adaptively. The 1-TDVP algorithm projects the exact tangent vector $|X_A\rangle$ into the (MPS) tangent space $T_{|\Psi(A)\rangle}\mathcal{M}$, which is a subspace of $T_{|\Psi(A)\rangle}\mathcal{H}$. Inspired by this, we choose a larger subspace, which contains the components normal to the MPS tangent space, and hence can go beyond the manifold \mathcal{M} . Such an algorithm dubbed as 2-TDVP using two-site update is illustrated in Fig. S11(a). The idea is straightforward, we “glue” two physical indices of a pair of nearest sites, and the bond dimension is increased adaptively when we separate the two sites again after the evolution.

To be specific, in 2-TDVP the projected tangent vector becomes

$$\widetilde{\Phi}_A(B) = \sum_{i=1}^{N-1} \widetilde{\Phi}_A^i(B_i) = \sum_{i=1}^{N-1} \sum_{\{s_j\}} \text{Tr} \left\{ A_1^{L s_1} \cdots A_{i-1}^{L s_{i-1}} B_i^{s_i, s_{i+1}} A_{i+2}^{R s_{i+2}} \cdots A_N^{R s_N} \right\} |s_1 \cdots s_N\rangle, \quad (\text{S25})$$

where $B = (B_1, \dots, B_{N-1})$ and each B_i is now a rank-4 local tensor related to a pair of nearest sites i and $i + 1$. The linear subspace corresponding to 2-TDVP is exactly the space of all the two-site variations, denoted by $T_{|\Psi(A)\rangle}^{(2)}$. It can be checked that any one-site variation that spans the tangent space $T_{|\Psi(A)\rangle}\mathcal{M}$ can be regarded as a special two-site variation. In this sense, $T_{|\Psi(A)\rangle}^{(2)}$ is indeed a larger subspace, i.e., we have the following rigorous relation

$$T_{|\Psi(A)\rangle}\mathcal{M} \subset T_{|\Psi(A)\rangle}^{(2)} \subset T_{|\Psi(A)\rangle}\mathcal{H}. \quad (\text{S26})$$

Following the same line as in the derivation of 1-TDVP, we introduce the left-orthogonal condition of tangent vectors as

$$\sum_{s_i} A_i^{s_i \dagger} B_i^{s_i, s_{i+1}} = 0, \quad (\text{S27})$$

which is illustrated in Fig. S11(b). The corresponding Lagrangian now reads

$$\mathcal{L} = \langle B_i, B_i \rangle - \langle B_i, X_i \rangle - \langle X_i, B_i \rangle + \sum_{\alpha, \beta, s_{i+1}} \lambda_{\alpha\beta}^{s_{i+1}} \sum_{s_i, \gamma} \overline{(B_i)_{\gamma\alpha}^{s_i, s_{i+1}}} (A_i^L)_{\gamma\beta}^{s_i}, \quad (\text{S28})$$

where X_i is a two-site tensor with the same size of $B_i^{s_i, s_{i+1}}$. Solve this extremum value problem and we arrive at

$$(B_i)_{\alpha\beta}^{s_i, s_{i+1}} = (X_i)_{\alpha\beta}^{s_i, s_{i+1}} - \sum_{s'_i, \gamma, \delta} \overline{(A_i^L)_{\delta\gamma}^{s'_i}} (X_i)_{\delta\beta}^{s'_i, s_{i+1}} (A_i^L)_{\alpha\gamma}^{s_i}, \quad (\text{S29})$$

see Fig. S11(c). If the tangent vector is induced by imaginary-time evolving equation in particular, then the flow equation of local tensors reads

$$\frac{dC_i}{d\beta} = -H_i^{(2)} C_i + A_i^L H_{i+1}^{(1)} A_{i+1}, \quad (\text{S30})$$

where $C_i = A_i^L A_{i+1}$ is the local two-site tensor and $H_i^{(2)}$ denotes the two-site effective Hamiltonian acting on site i and $i + 1$. Overall, instead of N 1-site update plus $(N - 1)$ bond update operations as in 1-TDVP, the 2-TDVP now involves $(N - 1)$ 2-site updates and $(N - 2)$ 1-site updates.

H. Lanczos-based exponential method

Take the 1-TDVP as an example, after the splitting in Sec. II E, we need to integrate the flow equation Eq. (S24) and compute $A_i(\beta) = e^{-H_i^{(1)}(\beta - \beta_0)} A_i(\beta_0)$ and $S_i(\beta) = e^{H_i^{(0)}(\beta - \beta_0)} S_i(\beta_0)$. Note that $H_i^{(1)}$ is a rank-6 tensor acting on the rank-3 local tensor A_i and can be regarded as a $D_{i-1} D_i \tilde{d}_i \times D_{i-1} D_i \tilde{d}_i$ matrix. The computational complexity of brute-force exponential method is very high and scales as $O(D^6)$, which can be greatly reduced to $O(D^3)$ via the Lanczos exponential technique as we actually only need to compute $e^{-H_i^{(1)}(\beta - \beta_0)} A_i(\beta_0)$ instead of $e^{-H_i^{(1)}(\beta - \beta_0)}$ explicitly.

The details of Lanczos-based exponential method are as follows. We take b as the initial state in a Hilbert space and H is an Hermitian operator acting on it. The key point of Lanczos exponential is to project the operator to the Krylov space

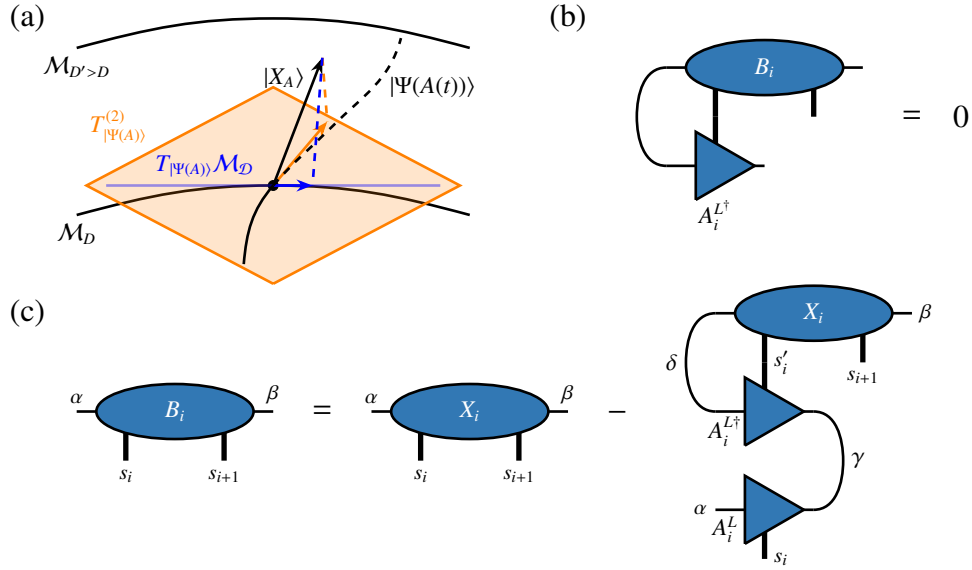


FIG. S11. (a) illustrates the comparison between 2-TDVP and 1-TDVP. Note that we plot the manifold \mathcal{M}_D of MPS with bond dimension D as a 1D manifold for the sake of convenience, and its tangent space $T_{|\Psi(A)\rangle}\mathcal{M}_D$ is depicted by a blue line. The space of 2-site variations $T_{|\Psi(A)\rangle}^{(2)}$ is a linear subspace of $T_{|\Psi(A)\rangle}\mathcal{H}$ which is strictly larger than $T_{|\Psi(A)\rangle}\mathcal{M}_D$, represented by the orange plane. The black arrow denotes the exact tangent vector $|X_A\rangle \in T_{|\Psi(A)\rangle}\mathcal{H}$, and the blue and orange arrows are the projection to $T_{|\Psi(A)\rangle}\mathcal{M}_D$ or $T_{|\Psi(A)\rangle}^{(2)}$, respectively. In 1-TDVP, the quantum-state/density-operator flow is induced by the blue tangent vector and hence the state cannot leave the manifold \mathcal{M}_D . However, the orange tangent vector has components normal to $T_{|\Psi(A)\rangle}\mathcal{M}_D$, hence the flow in 2-TDVP can leave the manifold \mathcal{M}_D and explore a manifold of larger bond dimensions, as illustrated by the dashed black curve. (b) shows the left-orthogonal condition of local tensor B_i in the 2-TDVP, and (c) shows the tensor network representation of the determined optimal two-site tensor B_i .

$\mathcal{K} \equiv \text{span}\{b, Hb, \dots, H^{K-1}b\}$, where K the Krylov space dimension. Through the standard Lanczos procedure, we find a group of orthogonal basis $\{q_i\}_{i=1}^K$ and the representation $H \approx QTQ^\dagger$ where $Q = [q_1, \dots, q_K]$ and T is a tridiagonal matrix. Given the Krylov space constructed, the exponential can be calculated as $e^H b \approx Qe^T Q^\dagger b = \|b\| \sum_{i=1}^K c_i q_i$ where the coefficients c_i 's constitute the first column of e^T . Note b is the initial vector of the Lanczos procedure and $q_1 = b/\|b\|$.

In the Lanczos procedure, we need to apply $H : v \mapsto Hv$ iteratively, whose computational complexity is $O(D^3)$. In Fig. S12 we illustrate the details of the tensor contractions involved in the 1-site update: we firstly contract L_i and A_i , then apply H_i to it, and finally contract the resultant with R_i . The complexity is thus estimated as

$$O(D^3 D_H) + O(D^2 D_H^2) + O(D^3 D_H) = O(D^3 D_H). \quad (\text{S31})$$

Note that D_H is the bond dimensions of the Hamiltonian MPO, which is much smaller than D in most cases involved in the present work. Besides 1-site update, the processes of bond and 2-site updates are similar and both of them are also with $O(D^3)$ complexity.

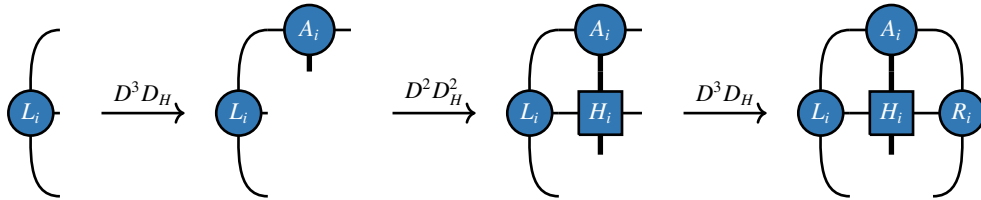


FIG. S12. The tensor contraction of $H_i^{(1)} A_i$ with $O(D^3)$ complexity in 1-site update.

III. Determinant Quantum Monte Carlo Simulations

In this section, we briefly recapitulate the determinant quantum Monte Carlo (DQMC) [68–71] method involved in the calculations. Below, we consider the square-lattice Hubbard model $H = H_0 + H_1$, where the kinetic energy H_0 and the on-site

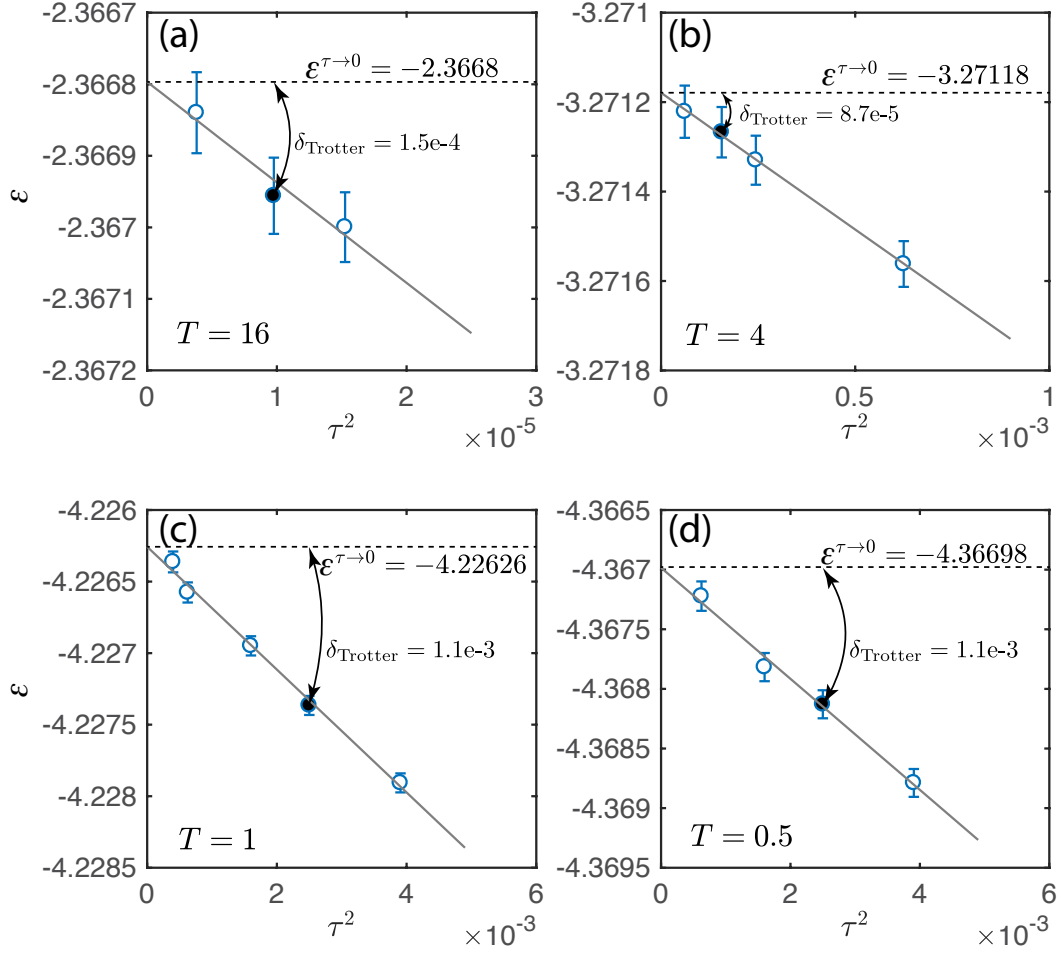


FIG. S13. In a $CL8 \times 16$ system with $U = 8$, DQMC energies density ε are shown versus the square of Trotter slices τ^2 for (a) $T/t = 16$ (b) $T/t = 4$, (c) $T/t = 1$, (d) $T/t = 0.5$, from which linear extrapolations on τ^2 are performed. For the data shown in the main text (solid dots), the corresponding Trotter errors are $\delta_{\text{Trotter}} = 1.5 \times 10^{-4}$, 8.7×10^{-5} , 1.1×10^{-3} , 1.1×10^{-3} .

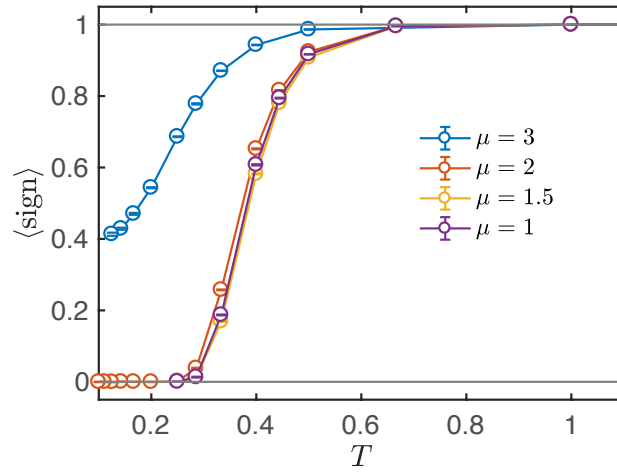


FIG. S14. In a $CL8 \times 16$ system with $U = 8$, the average signs $\langle \text{sign} \rangle$ are shown versus T for different chemical potentials μ , which show rapid decay to 0 around $T = 0.4$ for the cases of $\mu = 1, 1.5, 2$.

repulsion term H_I express as

$$H_0 = -t \sum_{\langle i,j \rangle, \sigma} (c_{i,\sigma}^\dagger c_{j,\sigma} + \text{H.c.}) = -t \sum_{i,j,\sigma} c_{i,\sigma}^\dagger K_{ij} c_{j,\sigma}, \quad H_I = U \sum_i (n_{i\uparrow} - \frac{1}{2})(n_{i\downarrow} - \frac{1}{2}), \quad (\text{S32})$$

with the matrix elements $K_{ij} \neq 0$ only if i and j are nearest-neighbor sites. The thermal density operator at inverse temperature $\beta \equiv 1/T$ can be approximated via the Trotter-Suzuki decomposition [90, 91] as,

$$\rho = e^{-\beta H} = (e^{-\tau H})^M \approx (e^{-\tau H_0} e^{-\tau H_I})^M, \quad (\text{S33})$$

where small imaginary time slice $\tau = \beta/M$ is taken to ensure sufficiently small Trotter error $\sim O(\tau^2)$ due to the fact $[H_0, H_I] \neq 0$. For the interaction term, we make use of the discrete form of Hubbard-Stratonovich (HS) transformation [69],

$$e^{-\tau H_I} = \prod_i e^{-\tau U (n_{i\uparrow} - \frac{1}{2})(n_{i\downarrow} - \frac{1}{2})} = \prod_i e^{\tau \frac{U}{2} (n_{i\uparrow} - n_{i\downarrow})^2 - \tau \frac{U}{4}} = \prod_i \gamma \sum_{s_i = \pm 1} e^{\alpha s_i (n_{i\uparrow} - n_{i\downarrow})} = \gamma^N \sum_{\{s_i = \pm 1\}} e^{\sum_i \alpha s_i (n_{i\uparrow} - n_{i\downarrow})}, \quad (\text{S34})$$

with N the total number of sites, $\gamma = \frac{1}{2} e^{-\tau U/4}$, and $\cosh \alpha = e^{\tau U/2}$. That is, the exponential of four-fermion terms are transformed to the exponential of two-fermion terms coupled to the (HS) ‘‘field’’ $\{s_i\}$. The many-body partition function thus writes

$$\mathcal{Z} = \text{Tr}(e^{\beta H}) \approx \text{Tr}[(e^{-\tau H_0} e^{-\tau H_I})^M] = \gamma^{NM} \sum_{\{s_i^l\}} \text{Tr} \left[\prod_{l=1}^M \left(e^{-\tau \sum_{i,\sigma} c_{i,\sigma}^\dagger K_{ij} c_{j,\sigma}} e^{\sum_i \alpha s_i^l (n_{i\uparrow} - n_{i\downarrow})} \right) \right] \quad (\text{S35})$$

$$= \gamma^{NM} \sum_{\{s_i^l\}} \text{Det} \left[I + \prod_{l=1}^M (e^{-\tau K} \cdot e^{\Lambda_l^\uparrow}) \right] \times \text{Det} \left[I + \prod_{l=1}^M (e^{-\tau K} \cdot e^{\Lambda_l^\downarrow}) \right], \quad (\text{S36})$$

where I is an $N \times N$ identity matrix, and Λ_l^\uparrow and Λ_l^\downarrow are diagonal matrix with the i -th entry being αs_i^l and $-\alpha s_i^l$ respectively. We assign each configuration C of $\{s_i^l\}$ with a weight

$$W_s(C) = \frac{\gamma^{NM}}{\mathcal{Z}} \text{Det} \left[I + \prod_{l=1}^M (e^{-\tau K} \cdot e^{\Lambda_l^\uparrow}) \right] \times \text{Det} \left[I + \prod_{l=1}^M (e^{-\tau K} \cdot e^{\Lambda_l^\downarrow}) \right], \quad (\text{S37})$$

and the thermodynamics of the Hubbard system is then reformulated into the summation over $N \times M$ Ising field $\{s_i^l\}$, with i labeling the site and l the imaginary-time slice. In Markov chain Monte Carlo, we consider the relative weights between configurations, and thus for each configuration we instead calculate

$$\tilde{W}_s(C) = \text{Det} \left[I + \prod_{l=1}^M (e^{-\tau K} \cdot e^{\Lambda_l^\uparrow}) \right] \times \text{Det} \left[I + \prod_{l=1}^M (e^{-\tau K} \cdot e^{\Lambda_l^\downarrow}) \right], \quad (\text{S38})$$

and use this relative weights to update Ising configurations.

To sum up, we provide the workflow of the Markov chain samplings in the DQMC below.

1. *Initialization*—We start with an initial random configuration C of the HS field $\{s_i^l\}$ and calculate its weight $\tilde{W}_s(C)$.
2. *Proposal of local updates*—At site 1 and imaginary-time slice 1, we flip the sign of the HS field, i.e. $(s_1^1)' = -s_1^1$.
3. *Accept/Decline*—We calculate the associated weight $\tilde{W}_s(C')$, accept or decline the local update according to the ratio $\frac{\tilde{W}_s(C')}{\tilde{W}_s(C)}$ of the weights.
4. *Full sweep*—We repeat step 2 and 3, for each site i from 1 towards N and for each slice l from 1 towards M . After that, we call it a full sweep of the configuration.
5. *Measurement*—For each fixed configuration of HS field $\{s_i^l\}$, the measurement of observable \hat{O} can be conducted like in an interaction-free fermion system.
6. We repeat the full sweep process N_{warm} times to thermalize the systems, and after that take N_{measure} times ‘‘full sweep + Measurement’’ procedures to collect N_{measure} measurements of the observables.

In practical calculations, we set $(N_{\text{warm}}, N_{\text{measure}}, N_{\text{chain}}) = (1000, 5000, 300)$ for the half-filled cases and up to $(1000, 5000, 500)$ for the doped cases, where N_{chain} is the number of Markov chains. I.e., we totally have 1,500,000 measurements at half-filling cases and 2,500,000 measurements at the doped cases for each observable. In the main text, we take $\tau = 0.05$ for the $T/t \leq 1$ cases, and take $\tau = \beta/20$ for the higher- T cases, rendering the Trotter errors within the order $O(10^{-3})$. In Fig. S13, we explicitly show the energies density u obtained from DQMC simulations versus the Trotter slice τ^2 for two different temperatures $T/t = 1/16, 1/4, 1, 0.5$ from panel (a) to (d). It can be seen that, the relative difference between the energies shown in the main text (indicated as the black filled dots) $\tau = 0.05$ and the extrapolated values ($\tau \rightarrow 0$) are within the order $O(10^{-3})$.